Available online at www.sciencedirect.com
SCIENCE DIRECT®
Journal of Hydrology 305 (2005) 15–39
Journal of Hydrology
www.elsevier.com/locate/jhydrol

Distributed hydrological model for mapping evapotranspiration using remote sensing inputs

Jing M. Chen[a,*], Xiaoyong Chen[a], Weimin Ju[a], Xiaoyuan Geng[b]

[a]*Department of Geography and Program in Planning, University of Toronto, 100 St. George Street, Room 5047, Toronto, Ont., Canada M5S 3G3*
[b]*Canada Centre for Remote Sensing, 588 Booth Street, Ottawa, Ont., Canada K1A 0Y7*

Received 8 July 2003; revised 30 June 2004; accepted 19 August 2004

Abstract

A distributed hydrological model [Wigmosta, M.S., Vail, L.W., Lettenmaier, D.P., 1994. A distributed hydrology-vegetation model for complex terrain. Water Resource Research 30 (6), 1665–1679] is further developed to simulate the detailed spatial and temporal variation patterns of evapotranspiration (ET) around a flux tower site. In addition to meteorological, topographical and soil data, the model utilizes optical remote sensing data (Landsat TM at 30 m resolution) to characterize the distributions of vegetation types and the leaf area index (LAI). The use of LAI allows process-based modeling of major hydrological processes including transpiration, precipitation interception, and evaporation from vegetation and soil. Water flows within and between five strata (overstore, understore, moss/litter, soil unsaturated zone, and soil saturated zone) are modeled on a daily basis. A moving window of nine pixels is used to consider the lateral subsurface flow. The model is applied to a small watershed of dimension of about 16 km×12 km in Saskatchewan, Canada. The temporal variations of simulated ET are compared with eddy-covariance ET measurements over a black spruce stand located within the watershed. The stand was the Old Black Spruce in the Southern Study Area during the Boreal Ecosystem-Atmosphere Study (BOREAS) in 1994. Although the black spruce site is located in a flat area with less than 1.5 m topographical variation within 150 m of the flux tower, there was about 10.5 mm water loss through saturated subsurface flow during the growing season of 1994, accounting for 5.7% of the rainfall in same period. Even though the watershed studied had gentle terrain variations, the topography had considerable influence not only on the water table but also on the soil moisture and saturated water redistribution. This suggests the importance of modeling hydrological processes as influenced by topography in mapping ET.

Keywords: Evapotranspiration; Subsurface flow; Water table; Soil moisture; Remote sensing; Watershed hydrology

Abbreviations: REA, Representative Elemental Areas; HRU, Hydrological Response Unit; GRU, Grouped Response Units; ASA, Aggregated Simulation Areas; BOREAS, Boreal Ecosystem-Atmosphere Study; OBS, Old Black Spruce; LAI, Leave Area Index; RHESSYS, Regional Hydro-Ecological Simulation System; ET, Evapotranspiration; DEM, Digital Elevation Model; SSA, Southern Study Area; DN, Digital Number.

* Corresponding author. Tel.: +1 416 978 7085; fax: +1 416 946 3886.
E-mail address: chenj@geog.utoronto.ca (J.M. Chen).

0022-1694/$ - see front matter © 2004 Elsevier B.V. All rights reserved.
doi:10.1016/j.jhydrol.2004.08.029

1. Introduction

Water is not only an important natural resource but is also critical in determining forest distribution and productivity. It should, therefore, be an integral part of terrestrial carbon cycle models (Baldocchi, 1997; Williams et al., 1997; Van Wijk et al., 2001). In order to improve our previous ecosystem model (Liu et al., 2002), in which the soil water budget is estimated based on a bucket model, we adopted and improved a distributed hydrological model (Wigmosta et al., 1994) to consider the influence of the lateral water flow on the spatial distribution of forest productivity. The focus of the present study is on the methodology of using remotely sensed data for hydrological modeling, a critical step in achieving our goal of investigating coupled water and carbon cycles in terrestrial ecosystems under the influence of topography. Soil water affects evapotranspiration and canopy photosynthesis, and hence net primary productivity (NPP) (Running and Hunt, 1993), and also influences the decomposition of soil organic matter (Parton et al., 1993). Current values of NPP and decomposition, in turn, are critical inputs to models for assessing the long-term carbon dynamics in forest ecosystems (Chen et al., 2000). However, hitherto, most (if not all) carbon cycle models applied at regional and global scales have not included three-dimensional hydrological processes, and soil moisture has been estimated using bucket models, without considering lateral exchanges of water among neighboring spatial units identified by remote sensing pixels. Our goal is to model coupled water and carbon cycles in terrestrial ecosystems so as to improve the understanding of the interactions between ecosystems and the climate.

In modeling hydrological cycles, we often encounter the problem of the large spatial and frequent temporal variations in hydrological processes. Compared with lumped models (Nash and Gleick, 1991; Mimikou et al., 1991; Mohseni and Stefan, 1998), distributed hydrological models can account for spatial heterogeneities and provide detailed descriptions of the hydrological processes in a watershed to satisfy various needs in spatial modeling (Abbott and Refsgaard, 1996). Distributed models are far less prone to calibration and extrapolation problems than lumped models (Zhang et al., 2000), but the main problems in their application are often the high demands on input spatial datasets and computation resources.

Many distributed hydrological models are developed for practical purposes of simulating and predicting runoff and hydrographs. In order to capture the major spatial variability while making models computationally efficient and overcoming problems with insufficient data, various numerical schemes have been used in several models. Wood et al. (1988) proposed the use of 'Representative Elemental Areas' (REA) for distributed hydrological modeling. Donald (1992); Kite and Kouwen (1992) used the 'Hydrological Response Unit' (HRU) based on land cover, slope and aspect for estimating the response of hydrographs to precipitation. Kouwen et al. (1993) further improved the computational efficiency by using 'Grouped Response Units' (GRU) in a regular grid system for estimating runoff to a stream and river network. For convenience and efficiency in modeling, Kite (1995) separated a watershed into 'Aggregated Simulation Areas' (ASA), which can be delineated as irregular shapes according to the hydrological characteristics within a watershed. All these numerical schemes were developed with the main purpose of computational efficiency. For simulating hydrographs, it is most important to capture the first order spatial variability. The gains in modeling accuracy diminish quickly as more spatial details are added, because uncertainties introduced by errors in spatial datasets and in model parameterization may exceed the gains in capturing the detailed spatial variability.

However, hydrological research is not confined to the needs of runoff simulation and prediction. It has, in fact, evolved to embrace broad science objectives, such as land-atmosphere interaction, and energy and mass transport within terrestrial systems (Engman, 1996). In our efforts to understand the impact of climate change on terrestrial ecosystems and on the global carbon cycle, it has been increasingly recognized that water and carbon cycles need to be modeled simultaneously (Field et al., 1998; Williams et al., 2001). The model developed through our present study serves the needs of (i) simulating water, energy and carbon fluxes measured at micrometeorological towers on non-flat terrains for model validation purpose, and (ii) simulating the spatial variations of water and carbon fluxes with topography for the purpose of scaling from tower to region. To meet these needs, it is

highly desirable to simulate water flow and balance in fine grids compatible with the surface variability. We, therefore, need to develop a hydrological model to capture the spatial variability in sufficient detail. This development is in the opposite direction to the spatial aggregation schemes mentioned above.

Remote sensing techniques, which inherently have the ability to provide spatial and temporal information of the land surface, may be the only viable way to obtain the data needed for distributed process models (Engman, 1996; Ritchie and Rango, 1996). The application of remote sensing techniques in hydrological studies and water resources management has progressed in the past decades (see review by Kite and Pietroniro, 1996). In general, remote sensing data are used in the following ways (Ritchie and Rango, 1996; Kite and Pietroniro, 1996; Schultz, 1996): (i) original remote sensing imagery is directly used to identify hydrologically significant areal phenomena, such as flooded areas (Barber et al., 1997; Brivio et al., 2002; Islam and Sado, 2002), snow cover (Baumgartner and Apfl, 1994; Tait et al., 2000) or plumes (Ouillon et al., 1997); (ii) processed remote sensing data are used to provide fields of hydrological parameters, such as precipitation (Kite and Pietroniro, 1996; Wang et al., 2001), and soil moisture (Jackson, 1993; Hollenbeck et al., 1996; Kim and Barros, 2002). This requires the understanding and development of relationships between electromagnetic signals and hydrological parameters of interest; and (iii) multispectral remote sensing data are used to quantify surface parameters, such as vegetation (land cover) types and density. Although the usefulness of remote sensing data is widely recognized, there remain few cases where remote sensing data have been actually used in hydrological simulations. Difficulties still exist in choosing the most suitable spectral data for studying hydrological processes as well as in interpreting such data to extract useful information (Abbott and Refsgaard, 1996; Kite and Pietroniro, 1996; Engman, 1996).

Among remotely sensed, hydrologically significant, variables that are under-utilized, are vegetation parameters derived from optical remote sensing. In particular, vegetation structural parameters, such as leaf area index (LAI), can play an important role in precipitation interception and evapotranspiration, and thus the water balance of a watershed. The Regional Hydro-Ecological Simulation System (RHESSys) (Band et al., 1993) made effective use of LAI and land cover derived from high-resolution, remote sensing images. These remotely derived variables were draped on watershed topography to find hydrologically significant vegetation patches on hill slopes. These patches then became the basic unit on which energy and water components have been simulated, while the spatial variation on the hill slopes within the same patches has not been considered. Such hillslope patch-based modeling may be adequate for simulating runoff and is an improvement over the methods of REA, HRU, GRU, and ASA in terms of capturing the major spatial variability between the hill slopes. However, in many cases the variations within a patch on a sloping surface may be still considerable. Vegetation on a hill slope generally varies along the elevation gradient. In boreal ecosystems, for example, vegetation generally grows better near the top of the slope than near the bottom of the slope because water accumulation near the bottom generally causes water logging and impedes plant growth. In such a case, we need to separate upland from lowland vegetation, even on the same slope. High-resolution remote sensing provides the necessary data to quantify such important small-scale variations. It is highly desirable, therefore, to simulate the hydrological processes based on remote sensing pixels. The objectives of this study are: (i) to develop a distributed model with a capability of simulating the lateral water movement among neighboring pixels under the influence of topography; (ii) to model the various hydrological components including precipitation interception, throughfall, evapotranspiration (ET), water table, soil moisture, etc. based on optical remote sensing inputs; (iii) to apply the model to a forested watershed for the purpose of validating the ET calculation and mapping ET spatial distribution and seasonal variation patterns; and (iv) to estimate the effect of lateral subsurface flow on the water budget of a tower site located in the watershed.

2. Model description

In the present study, the physically based, distributed hydrology-vegetation model of Wigmosta et al. (1994) is adopted with several modifications. The complete model with modifications is presented in Appendix A.

The original Wigmosta's model provides an effective system to consider the flow of water in the soil-plant-atmosphere continuum, and is similar to many other models (Beven and Kirkby, 1979; Band et al., 1993; Paniconi and Wood, 1993). In addition, the model also includes a modeling framework in which the water flow is simulated among neighboring spatial units in a regular grid on varying topography. This framework is particularly suitable for applications to remote sensing data as pixels in remote sensing images can be treated as the spatial units.

2.1. Model structure and assumptions

The horizontal boundary of the simulated area is a watershed delineated from a digital elevation model (DEM) where divides between neighboring watersheds are identified. Vertically, the simulation extends from the saturated zone in the soil to the top of vegetation canopy. Within a watershed, the forest ecosystem is divided into basic spatial units, or pixels in remote sensing. Each pixel is treated as a unique vegetation–soil system, except for the ground and runoff water exchanges. Basic model simulations of the physical and biological processes are made at the pixel scale. According to the need of simulating hydrological processes, a pixel is vertically divided into five strata, i.e. overstorey, understorey, litter or moss layer, soil unsaturated zone, and soil saturated zone (Fig. 1). Precipitation, solar radiation, topographic parameters, land cover, leaf area index (LAI), and soil properties are the major inputs to the model. All input parameters are spatially resampled to a common resolution, which is 30 m × 30 m in this

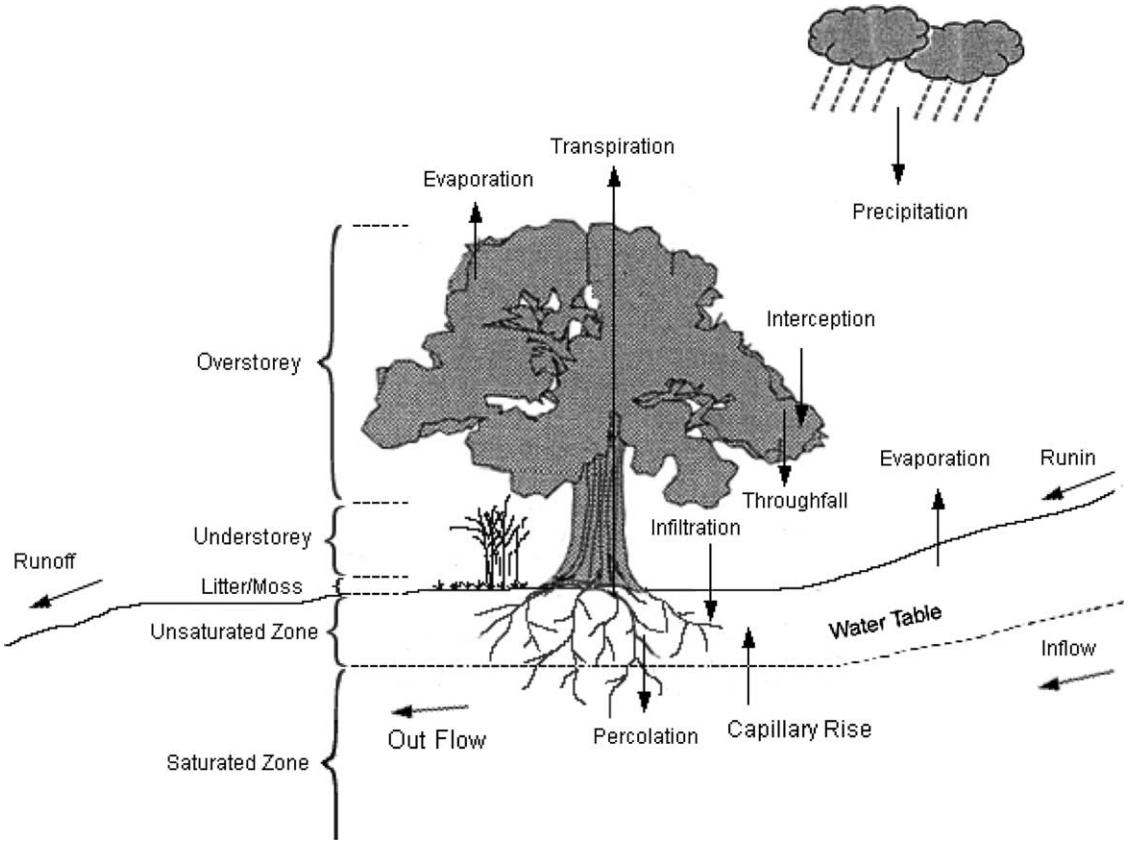

Fig. 1. Major hydrological components considered in the modeling system consisting of five strata: overstorey, understorey, litter/moss, unsaturated zone and saturated zone. Each remote sensing pixel is considered as a unique model system.

study to be compatible with Landsat TM images. The use of remotely derived parameters, such as LAI and land cover, allows for process-based modeling of evapotranspiration (ET) using the Penman–Monteith equation (Monteith, 1965) as well as other hydrological and energy components such as precipitation interception and its evaporation. The major outputs are ET, soil moisture, and water table. The framework of the model, separated into input, main model and output domains, is illustrated in Fig. 2. Horizontally, a moving window of 3×3 pixels is used to estimate the lateral, saturated, base flow according to topography and water table (Fig. 3), based on a set of equations (Eqs. (A27) and (A28)) described in the Appendix A.6. At each daily time step, this window is moved across the modeling domain to update the water table of each pixel as a result of the net lateral base flow in all eight cardinal directions. As the hydraulic conductivity in saturated soils is generally less than

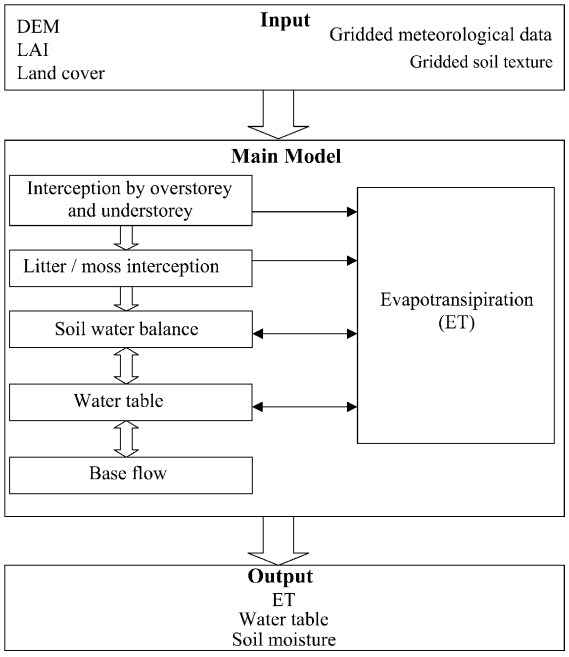

Fig. 2. Inputs and outputs of the model, and major processes affecting evapotranspiration (ET). Soil moisture changes are determined by estimating the soil water balance at daily time step. Both soil moisture and the water table affect ET because the water table can seasonally rise to within the root zone. ET in turn affects both soil moisture and water table. The spatial variation of water table causes the saturated base flow.

X= 1 i-1,j-1	X= 2 i-1,j	X= 3 i-1, j+1
X= 8 i,j-1	X i,j	X= 4 i,j+1
X= 7 i+1, j-1	X= 6 i+1,j	X= 5 i+1,j+1

Fig. 3. Relationship of a central pixel ($X_{i,j}$) with its eight neighboring pixels for saturated subsurface flow routing (described by Eqs. (A27) and (A28)).

1 m d^{-1} (Ward and Robinson, 2000), the daily time step is adequate for estimating the lateral water flow for 30 m×30 m pixels.

Several major assumptions are made in the model: (i) all physical and biological properties are homogeneous within the basic modeling unit, i.e. the pixel; (ii) soil texture is vertically invariant (although structure changes with depth); (iii) as the model is generally run at daily time steps, a sinusoidal diurnal variation pattern of the incident solar radiation is assumed in deriving daily radiation components (Eqs. (A53) and (A54)); and (iv) at the daily time step, surface runoff does not occur until the whole soil profile is saturated.

2.2. Modifications to Wigmosta's model

The general goal of the modifications we made to the model is to maximize the use of remote sensing data in both soil water and runoff modeling and to illustrate the variability in hydrological parameters at high spatial resolutions. The major modifications include: (i) a moss ground cover is introduced and its effect on ET is considered (Appendix A.2); and (ii) the effects of water logging on stomatal conductance and ET are considered (Appendix A.5). This modification is particularly relevant to the boreal environment where large portions of the landscape are waterlogged

or seasonally flooded; (iii) using a root vertical density distribution function, roots are distributed in both unsaturated and saturated soil zones depending on variation in the seasonal water table variation (Appendix A.6); and (iv) a comprehensive set of equations is developed to simulate direct, diffuse and net radiation in the overstorey, understorey and moss/soil surface (Appendix A.8). As the goal of our hydrological modeling is to quantify coupled water and carbon cycles, these modifications are essential to capture realistic spatial and temporal variation patterns of properties affecting these cycles in the boreal landscape.

The focus of the present study using the modified model is on simulating water storage in the soil and its effects on evapotranspiration. Water storage and movement in the soil are essential to the understanding of a wide range of hydrological processes, including the dynamics of infiltration and percolation, runoff generation, recharge to underlying groundwater, and water supply to plants. Water storage not only has hydrological significance but is also important in carbon cycle modeling as it also affects microbial activities responsible for decomposition of organic matter in the soil.

3. Site description and data preparation

The distributed model is applied to part of the Southern Study Area (SSA) of the Boreal Ecosystem-Atmosphere Study (BOREAS). The hydrological modeling domain encompasses the old black spruce (SSA-OBS) stand, about 30 km northeast of Candle Lake, Saskatchewan (53.987°N, 105.118°W), Canada. The climate is cold-temperate with the monthly temperature of 16.7 °C in July and −16.9 °C in January. The annual precipitation is approximately 400 mm. The soil originates predominantly from Glacial Lake Agassiz sediments and consists of sand, clay and organic matter. The topography has low relief and poor drainage (Nakane et al., 1997). The site for the present study comprises 532×405 pixels at 30 m resolution. The watershed studied here is in a typical Canadian shield landscape with gentle and moderate topographical variations on top of a shallow bedrock (Branfireun and Roulet, 1998). In the landscape, slopes with shallow overburden may be decoupled from receiving streams in dry seasons (Devito et al., 1996). This particular watershed drains to a small lake through saturated subsurface flows and ephemeral streams. We, therefore, emphasize the abilities of the model to capture spatial variation patterns of various parameters rather than runoff simulations, although Wigmosta's model was successfully used for simulating stream flows (Storck et al., 1998).

The forests within the modeling domain are typical of southern boreal forests, consisting primarily of black spruce (*Picea mariana* (Mill.) BSP) with small patches of jack pine (<2% in tree count) (*Pinus banksiana* Lamb.), and other tree species (<3%) including tamarack (*Larix laricina* (Du Roi) K. Koch) and willow (*Salix* spp.) (Gower et al., 1997). The basal area of the stands at the OBS site is 30 $m^2\,ha^{-1}$ (Jarvis et al., 1997) and the average leaf area index (LAI) is 4.5 (Chen et al., 1997). The understorey is composed of grasses of variable densities and sparse shrubs above an extensive moss ground cover. The growing season is normally limited to the summer months between May and September when the daily temperature is above 5 °C. As the effect of lateral water flows on ET is the main focus of this study, we intensively investigated ET and associated hydrological parameters during the growing season in 1994.

Various spatial datasets were pre-processed as inputs to the model. They include: (i) slope and aspect derived from a digital elevation model (DEM) dataset (16-bit unsigned integer raster file) for each pixel of the watershed with a spatial resolution of 30 m×30 m using ARC/INFO; (ii) meteorological data including precipitation, maximum, minimum and mean air temperatures, humidity, and radiation. These variables were measured at the OBS tower site (Jarvis et al., 1997) and treated in the same way for all pixels within this small watershed; and (iii) land cover and LAI maps derived from Landsat imagery which was geometrically and radiometrically pre-corrected. In the image processing, the digital numbers (DN) of the visible and infrared bands were converted into radiance and reflectance after an atmospheric correction procedure. Land cover classification was based on Cihlar et al. (1999), and LAI was calculated using the algorithms of Chen and Cihlar (1996); and (iv) soil attributes, including texture and water holding capacity, were obtained from a soil map at a scale

of 1:1,000,000 (De Jong et al., 1984; Acton et al., 1991). The map with soil polygons is rasterized to a 30 m × 30 m grid system in ARC/INFO. Water flux data (Jarvis et al., 1997) measured on the SSA-OBS tower and soil moisture data (Peck et al., 1997) measured near the tower are used for model validation.

The water table and soil moisture fields before the growing season were initialized using the TOPMODEL principle (Kirkby, 1975; Beven and Kirkby, 1979). The wetness index ($W_{i,j}$) for a pixel at (i,j) (Beven and Kirkby, 1979) was first calculated as:

$$W_{i,j} = \ln\left(\frac{A_{i,j}}{\tan\beta_{i,j} + 0.05}\right) \quad (1)$$

where $A_{i,j}$ is the contributing area calculated from the DEM using the ARCGIS FLOWACCUMULATION command, and $\beta_{i,j}$ is the slope. The initial water table ($z_{t,i,j}$) was then linearly related to the wetness index:

$$z_{t,i,j} = \bar{z}_t + m(W_{i,j} - \bar{W}) \quad (2)$$

where $\bar{z}_t$ is the mean water table taken as 0.35 m determined through a spin-up calculation for 1 year; and $\bar{W}$ is the mean wetness index determined to be 4 from the W image, and m was set at 0.7 m (Beaujouan et al., 2002). The soil moisture content in the unsaturated zone was set at 70% of the field capacity at the beginning of the growing season for all pixels.

4. Results and discussion

4.1. Spatial distribution of hydrological parameters

Spatially distributed hydrological parameters were first generated by the model based on topography. Fig. 4 shows the spatial distributions of DEM and wetness index. The initial values of water table and the mean soil moisture content (SMC) in the unsaturated zone at the beginning of the growing season have spatial distribution patterns similar to that of the wetness index. As the model is run at daily time steps, the water table and SMC were updated daily for any given pixel (30 m × 30 m) in the modeling domain. In many areas, the water table was near the surface all year round (wetland), and ET draws water from the saturated zone. Other areas are seasonally wet with fluctuating water tables. The modifications to

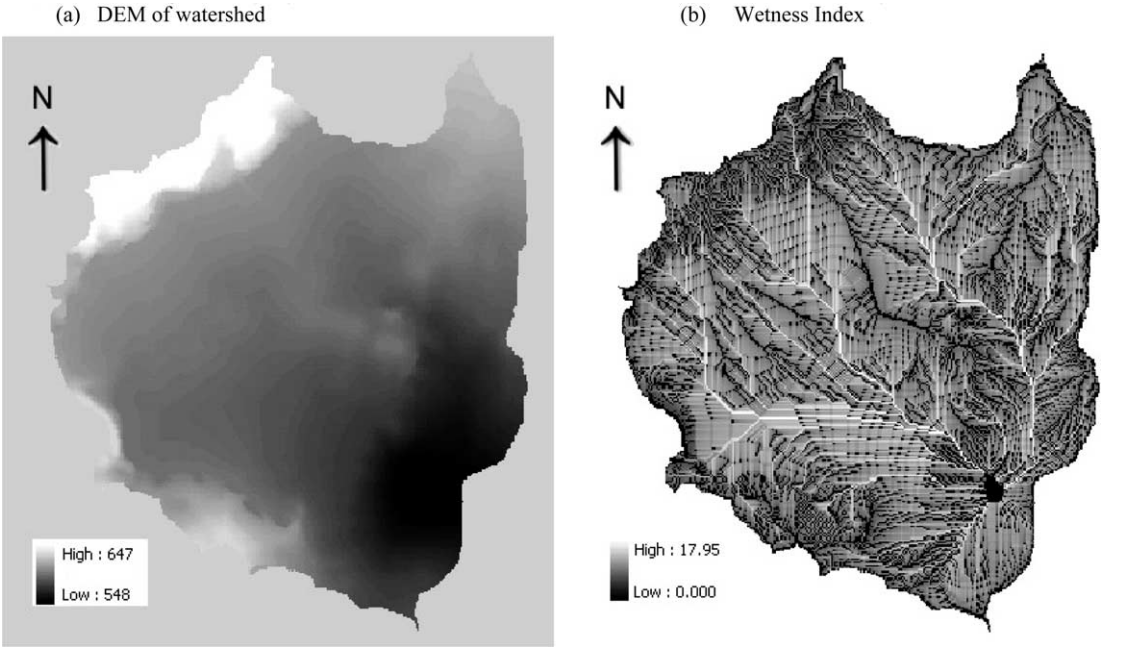

Fig. 4. The digital elevation model (DEM) of a small watershed draining toward a small lake near the bottom-right corner, and the wetness index calculated from the DEM using Eq. (1). This forest watershed is located on the boreal shield in Saskatchewan, Canada.

the original Wigmosta's model in terms of rooting depth and stomatal control under water logging conditions are therefore essential for application to the boreal environment.

Spatial distributions of LAI, land cover, and soil type are shown in Fig. 5, with these variables draped on a 3-dimensional topographical display. Also shown in Fig. 5(a) are the SSA-OBS site with tower flux data

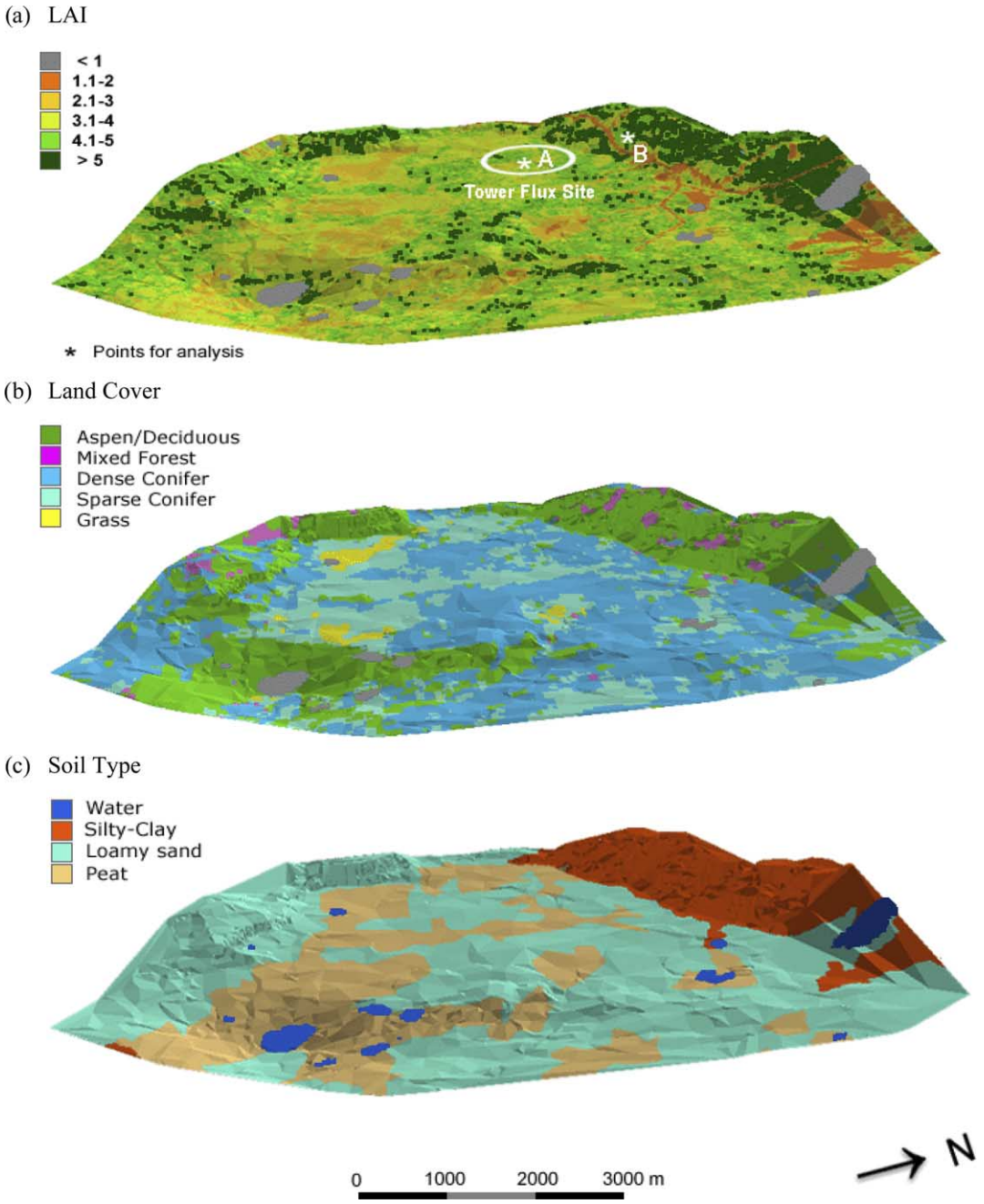

Fig. 5. LAI, land cover and soil type maps in the model domain draped on a 3-dimensional topographical visualization. The circle on the LAI map indicates the BOREAS SSA-OBS site (500 m radius) and points A and B are the low and high areas studied in Fig. 7.

in 1994 and selected locations A and B within the model domain for checking the model performance. There are marked resemblances among the spatial patterns of LAI, land cover and the soil texture, reflecting the fact that the soil texture map was originally obtained with the aid of photogrammetry.

4.2. Validation of modeled ET and soil moisture with measurements

The simulated and the measured daily evapotranspiration (ET) from an area (600×600 m^2) around the SSA-OBS tower site, for the days of 150–250 in 1994, are shown in Fig. 6. This area is considered to be adequate to represent the footprint area of the flux measurements (Schmid, 2002). The temporal patterns of the simulated and the measured daily evapotranspiration are similar, with no significant difference between them ($F = 0.423 < F_\alpha$, $\alpha = 0.01$). The simulated mean daily ET at the study site over the 100-day-period is 2.1 mm/day, comparable to the ET measurements taken at the site (Jarvis et al., 1997; Pattey et al., 1997). Using eddy covariance measurements taken at a height of 27 m above the ground, Jarvis et al. (1997) reported average daily ET of 2.07 mm/day for DOY 150 to DOY 250 in 1994. Pattey et al. (1997) presented eddy covariance data measured at a height of 20 m above ground for three intensive field campaigns during 1994. Their values of mean daily ET were 2.26, 3.32, and 1.44 mm/day for the periods of May 24–June 4, July 19–July 29, and September 8–17, respectively. Our modeled values were 2.31, 2.71 and 1.5 mm/day for the periods of June 1–10, July 19–29, and September 1–10, respectively.

ET is a critical factor determining the water balance in forest ecosystems, and is the major component of the water balance in Canadian forests. The Penman–Monteith equation is widely employed to estimate vegetation ET, and has been shown to be accurate and reliable (Roberts et al., 1993; Running and Coughlan, 1988; Landsberg and Waring, 1997; Mielke et al., 1999; Soares and Almeida, 2001). Our current results add further support to using the equation for ET estimation.

There were also a few soil moisture measurements during the growing season within the footprint area of the tower (Peck et al., 1997). Modeled daily soil moisture values near the tower (as an average of 20×20 pixels around the tower) are compared with these measurements (Fig. 7). The model agrees with the mid-summer measurements, but seems to underestimate soil moisture at the end of the growing season, although the data points are too few for a complete evaluation of model performance.

Lateral water flow at this site has a small but significant effect on the water balance and ET. For this purpose, we selected two concentric square areas:

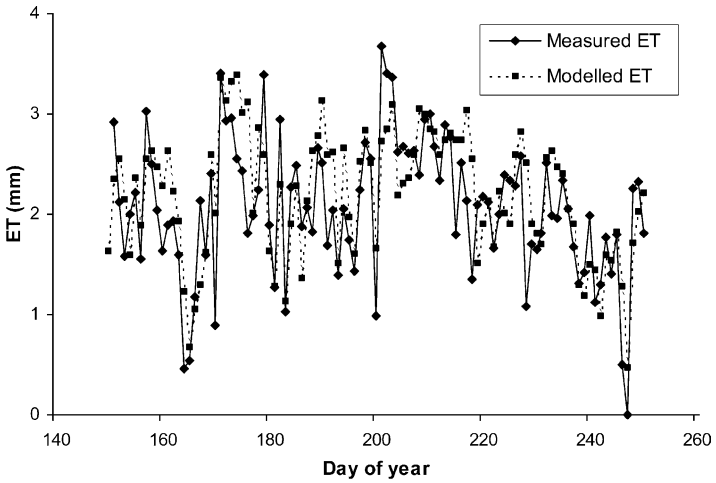

Fig. 6. Temporal variations of modeled evapotranspiration (ET) in comparison with eddy covariance ET measurements made on a tower in the BOREAS SSA-OBS site shown in Fig. 5 (Jarvis et al., 1997). The modeled values are averages of a 600 m $\times$ 600 m area centered on the tower.

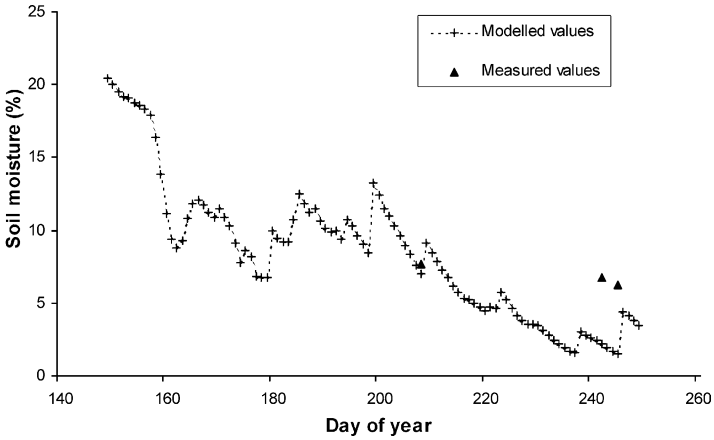

Fig. 7. Comparison of modeled volumetric soil moisture in the unsaturated zone (average of a 600 m×600 m area around the SSA-OBS flux tower) with three measurements near the tower.

Area 1 within about 150 m of the tower (10×10 pixels at 30 m resolution), and Area 2 within about 300 m of the tower (20×20 pixels). The site is relatively flat with only 1.23 and 3.35 m differences in DEM in Areas 1 and 2, respectively. However, these tower footprint areas receive ground water flows from adjacent higher ground and discharge to lower areas. The result of this lateral ground water exchange is a net loss of water of about 10.5 and 2.5 mm in the period of DOY from 150 to 250 for Areas 1 and 2, respectively. These lateral water losses are about 5.7 and 1.4% of the rainfall of 184 mm in the same period, respectively. This difference in the average water loss in these two areas reflects the fact that the tower is located in a relatively dry area. As distance increases from the tower, the area becomes progressively wetter. The mean wetness index is 7.6 and 8.3 in Areas 1 and 2, respectively. These modeling results indicate that although the tower flux site is located in a flat area in the boreal landscape (almost as flat as one can find), there is still significant ground water exchange, and bucket models that do not consider lateral ground water flow can cause errors in the water balance of up to 6% of the total rainfall.

4.3. Spatial distribution of evapotranspiration

To evaluate reliability of the distributed process model, a test on the model was done on the key parameters: soil moisture, ET and water table. In the model, the water table is defined as the depth from the surface at which the soil is saturated. Because of topographical variations, the water table should vary with local elevation in a predictable manner if the model performs correctly. We hypothesize that the water table should be the same at points with the same elevation in a flat area and that in the higher land areas lower elevation sites should have higher water tables (closer to the surface).

To test this hypotheses, Areas A and B (locations defined in Table 1 as averages of three pixels in a line, also shown in Fig. 5a) located in low and high areas, respectively, were chosen for evaluating the model performance. Soil moisture changed greatly during the growing season in these locations (Fig. 8a and b). The temporal dynamics of soil moisture matched the rainfall events very well: the larger the amount of rainfall, the larger the increase in soil moisture. The response of soil moisture to rainfall was stronger in the low area where the inflow of ground water was larger than the outflow and the unsaturated zone was shallower than that in the higher area. In both low

Table 1
Relative locations, elevations (m) and LAI values of areas A and B chosen to represent low and high areas, respectively

Point	Location (line, pixel)	Elevation (M)	LAI
A	174, 155–157	589.6	3.8
	175, 155–157	589.5	3.5
B	102, 153–155	631.7	4.6
	103, 153–155	628.7	4.8

Areas A and B are also shown in Fig. 5a.

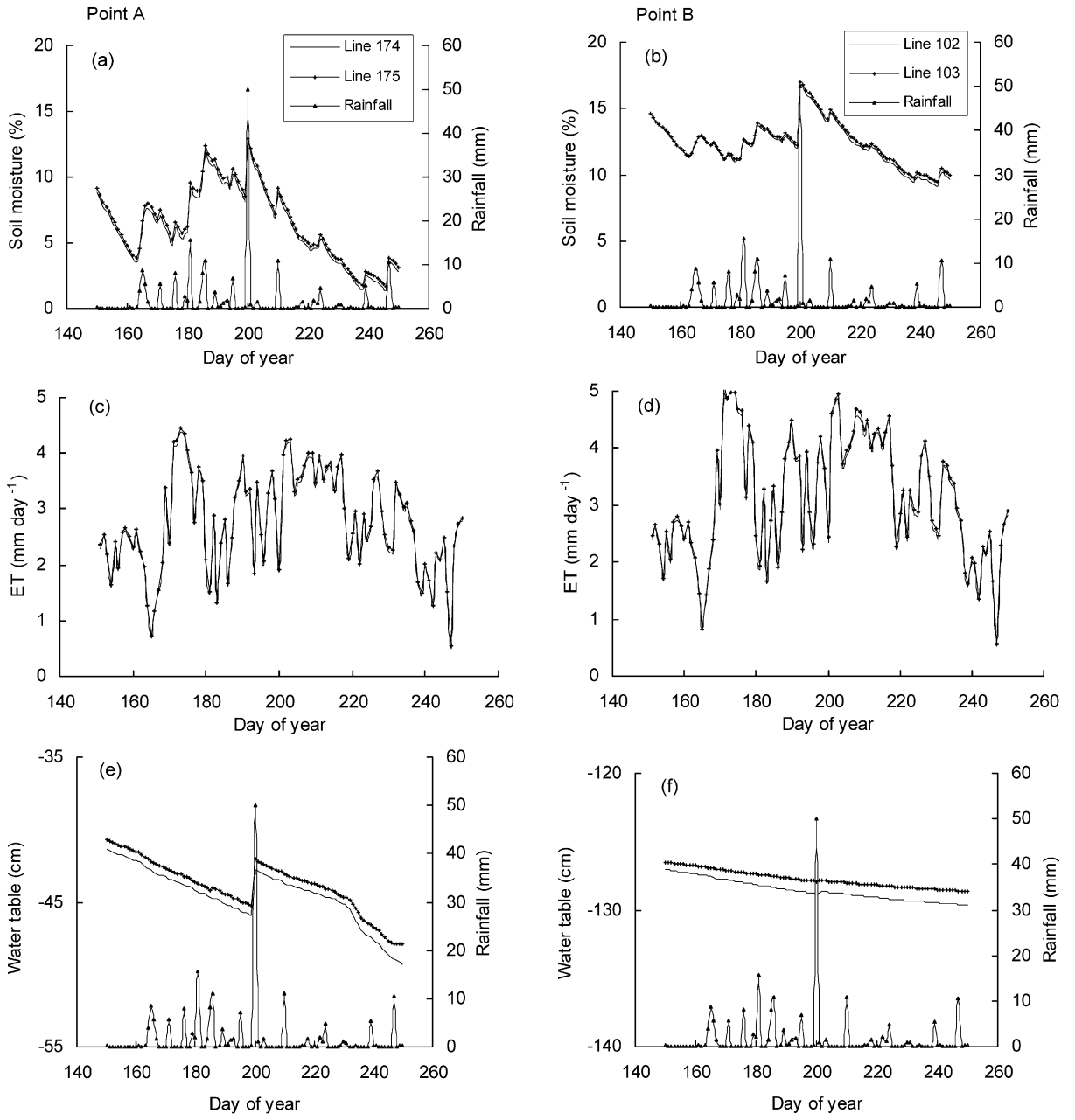

Fig. 8. Temporal variations of soil moisture, ET, and water table in Areas A and B representing low and high areas, respectively. The location, elevation and LAI of these areas are given in Table 1.

(Fig. 8a) and high areas (Fig. 8b), the differences in soil moisture were very small among neighboring pixels (line 174 and line 175, line 102 and line 103). The variations in ET between neighboring pixels were also very small (Fig. 8c and d). However, ET in the high area was considerably larger than that in the low area. The simulated water tables in low and high areas were shown in Fig. 8e and f. In both cases, there were

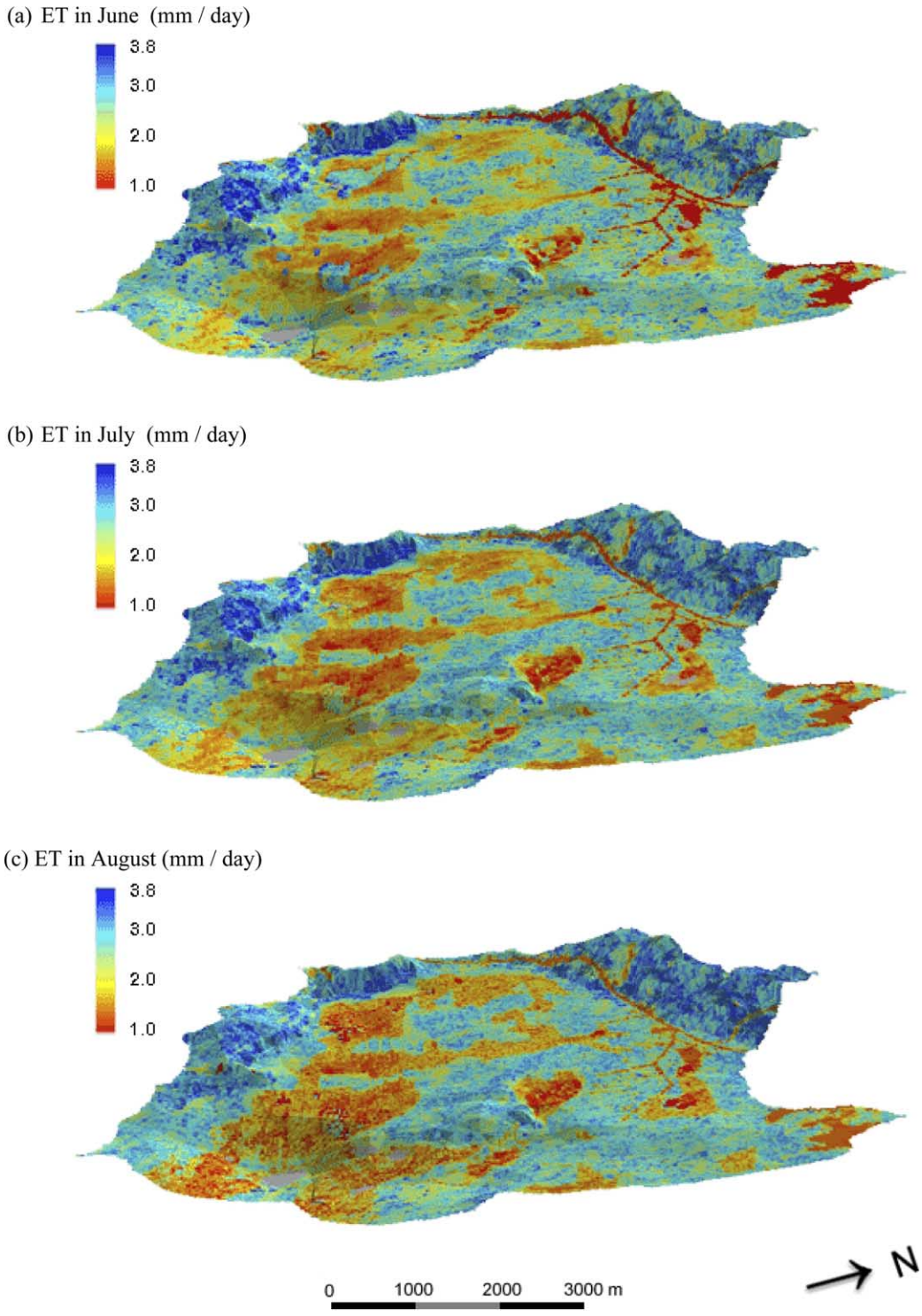

Fig. 9. Spatial distributions of the average daily evapotranspiration (ET) in the watershed in June, July, and August 1994. Line features represent roads.

small differences in water table between neighboring pixels. In the low area, with a shallow unsaturated zone, the water table had a pronounced response to large rainfall events, while in the higher area, the response was weak. As the growing season progressed from mid summer, both low and high areas became drier with decreasing soil moisture. The depth of the water table in the low area (Fig. 8e) decreased substantially with time, while it decreased slightly in the higher area as the result of slow water loss through lateral subsurface flow (Fig. 8f). The two adjacent lines of pixels separated by 30 m (line 102 and line 103) in the higher area developed a progressively larger difference in the water table during the growing season, indicating the sensitivity of water table depth to topography. The results indicate that the model is capable of simulating the lateral movement of water among pixels along the elevation gradient. Such a capability is critical in effective use of remote sensing for hydrological studies. From Fig. 8, it is noted that the influence of ET on the behavior of the water table was most significant in the areas with a shallow unsaturated soil layer (in lowlands). In areas with deeper water tables from the surface, ET had much smaller effects on the water table. Similarly, the impact of rainfall on soil moisture was strong in low areas with shallow unsaturated layers and weak in high areas with deep unsaturated layers. These results suggest that the size of the unsaturated zone is not only determined by the initial water table under the influence of topography, but also by ET under the control of surface and meteorological conditions.

The spatial distributions of the simulated ET for June, July and August are shown in Fig. 9. There are marked spatial variations in ET, corresponding to cover types and LAI distribution patterns as well as soil texture. Spatial variations in ET were weakest in June when soil moisture was high throughout the modeling domain and the available energy was also high. In July, the variations were strongest when the soil moisture increased or decreased non-uniformly because of ET and lateral water redistribution, and the available energy remained relatively high. In low areas, lateral water flows caused decreases in water table depth and ET, while frequent rainfall events sustained high soil moisture for ET in high areas. In August the variations were mostly controlled by soil moisture when both rainfall amount and available energy decreased considerably from June. These spatial–temporal dynamics have implications for obtaining spatially averaged values of ET or for interpreting tower ET measurements with large footprint areas. The ET spatial pattern is not only related to vegetation pattern but is also influenced by topography. As the water table temporal dynamics are also controlled by topography in a given rainfall event, mapping ET without considering the influence of topography is likely to lead to errors of different sizes at different times of the growing season. Similarly to the water table, soil moisture also shows distinct dynamics at different positions in the watershed, suggesting that carbon cycle modeling involving the effects of aerobic conditions on microbial activities would benefit from such topography-dependent soil moisture modeling.

5. Conclusions

A distributed hydrological model is further developed to simulate hydrological processes at high spatial resolutions and is applied to a small forested watershed located on a boreal precambrian shield. The modeling unit is a remote sensing pixel, rather than a hillslope or patch, so as to maximize the use of spatial information obtained from remote sensing to characterize both above-ground and below-ground variations along topographical gradients. After validating the model with available evapotranspiration (ET) and soil moisture data collected within the watershed, the following conclusions can be drawn:

(1) Spatially, there were large variations in ET across the watershed at any given time. Forest stands located in high areas generally have the highest ET, while seasonally flooded lower areas generally have the lowest ET. Relatively dry low areas have intermediate ET values. These spatial variation patterns closely follow vegetation cover types as well as leaf area index, both of which are highly correlated with the underlying soil type.
(2) Temporally, soil moisture in the unsaturated zone varies greatly with rainfall events, with the variation in low areas much larger than that in

high areas. Soil moisture in the unsaturated zone in low areas responded strongly to rainfall events because of the shallow water table and additional net inputs from lateral saturated subsurface flows. Short drought episodes also occurred between rainfall events, even causing short-term water stress in the relatively dry low areas.

(3) The lateral subsurface water flow resulted in a loss of about 5.7% rainfall during the growing season in a 300 m×300 m area surrounding the BOREAS OBS tower, even though the tower is located in a relatively flat area with only 1.23 m variation in elevation within the area. This suggests that ground water hydrology cannot be ignored around flux towers on variable terrain.

These conclusions suggest that it is indeed necessary to couple a carbon cycle model with a pixel-based hydrological model in order to study the spatial variability of carbon absorption and release as influenced by micro topography.

Acknowledgements

We are indebted to Prof. Paul Jarvis and his group at the University of Edinburgh and Drs. Ray Desjardins and Elizabeth Pattey of Agriculture and Agri-Food Canada for their kindness in allowing us to use their ET and soil moisture data for model validation. The initial modeling work was conducted at Canada Centre for Remote Sensing and was continued at the University of Toronto since 2000. The work was later supported by grants to J. M. Chen from the 973 program of Chinese Ministry of Science and Technology (grant # 2001CB309404), Natural Science and Engineering Council of Canada, and Canadian Foundation of Climate and Atmospheric Sciences. Mr Gang Mo provided valuable technical assistance at a later stage.

Appendix A. Modified Wigmosta's distributed hydrological model

We have adopted the principles of Wigmosta's model for vertical and horizontal water flow estimation and most of the equations based on the published paper (Wigmosta et al., 1994). However, we have also modified the original model in various ways. It is therefore necessary to give a complete description here as used in our study. The symbol '*' by an equation number indicates a modified equation from the original model, while '**' indicates a new equation.

A.1. Water budget within a pixel

The five-layer modeling domain is shown in Fig. 1. When precipitation (P) falls on the forest overstorey canopy, some is intercepted by the canopy (P_o), which is lost through subsequent evaporation. The difference ($P-P_o$) reaches the understorey, and part of it is intercepted by this layer (P_u). The net precipitation ($P_n = P - P_o - P_u$) wetting the soil surface infiltrates into the unsaturated soil zone. Surface runoff (R_s) occurs if P_n exceeds the soil maximum moisture capacity. Percolation begins during a rainfall event once the soil moisture content in the unsaturated zone is above field capacity.

The capillary fringe is treated as part of the saturated zone. The saturated zone is assumed to have an unlimited depth. The surface of the saturated zone can be measured by the local gravity drainage storage deficit (Beven and Kirkby, 1979), and the deficit is set to zero when the soil profile is fully saturated up to the surface. A negative value indicates water surplus, and the surplus would become part of surface runoff depending on topography. The subsurface flow was calculated non-linearly.

Based on the mass conservation principle, water balance of a vegetation/soil system in a pixel can be expressed using the following basic equation:

$$\Delta W_o + \Delta W_u + \Delta W_{unsat} + \Delta W_{sat} = P - E_o - E_u - T_o - T_u - R_s - E_s - W_{dr} \quad \text{(A1)*}$$

where ΔW_o, ΔW_u, ΔW_{unsat}, and ΔW_{sat} are the changes in water storage in the overstorey, understorey, soil unsaturated zone and soil saturated zone, respectively. P is precipitation; E_o is overstorey evaporation of intercepted rainfall; E_u is understorey evaporation of intercepted rainfall; T_o is actual transpiration from the overstorey; T_u is actual transpiration from

the understorey; R_s is surface runoff; E_s is actual soil evaporation; and W_{dr} is deep drainage. For simplicity, we treat the moss layer as a slab of living organisms that extract water directly from the unsaturated soil underneath through capillary transfer, and hence the moss and the unsaturated zone together is treated as a single layer from the water budget point of view. Methods to compute these variables are described in the following sections.

A.2. Water balances of overstorey and understorey in a pixel

Precipitation is intercepted by the overstorey and understorey layers. If the maximum interception capacities of these layers are reached, any excess precipitation is assumed to fall to the ground surface. The actual intercepted rainfall depends upon on the water storage at the beginning of each time step. The storage changes are estimated as follows:

$$\Delta S_{ti} = \min(P_{Ii} - S_{ti}, P_i) - E_{ai} \tag{A2}$$

where ΔS_{ti} is storage change of layer i representing the overstorey or understorey, S_{ti} is storage at the beginning of each time step, and E_{ai} is the actual evaporation of layer i. The maximum interception storage capacities (P_{Ii} in m) of these layers are determined as a function of leaf area index of the layer (L_i) and the proportion of the gaps in the layer (G_i) (Dickinson et al., 1991):

$$P_{Ii} = 10^{-4} L_i (1 - G_i) \tag{A3}$$

For these vegetation layers, evaporation and transpiration are calculated separately. Water detained in the canopy (wet vegetation surface) is assumed to be evaporated at a potential rate. Transpiration occurs from both dry and wet leaf surfaces. Both evaporation and transpiration rates can be estimated using the Penman–Monteith equation (Monteith, 1965):

$$E_{ti} = \frac{\Delta R_{ni} + \rho c_p \frac{e_s - e}{r_{ai}}}{\lambda_v \left(\Delta + \gamma \left(1 + \frac{r_{ci}}{r_{ai}}\right)\right)} \delta t \tag{A4}$$

where E_{ti} is the amount of water transpired from a layer over the time period T, R_{ni} is the net radiation of layer i, which is calculated with the absorbed shortwave and longwave energy (Eqs. (A45)–(A60)), ρ is density of moist air, c_p is the specific heat of air at a constant pressure, e_s is the saturated water vapor pressure, e is the actual air water vapor pressure, r_{ai} is the aerodynamic resistance to vapor transport for layer i, λ_v is the latent heat of vaporization of water, Δ is the slope of the saturated vapor pressure–temperature curve, γ is the psychrometric constant, and r_{ci} is the canopy resistance to vapor transport.

For the transpiration component, r_{ci} is estimated as follows

$$r_{ci} = \frac{1}{g_{si} L_i} \tag{A5}$$

where L_i is the leaf area index of the overstorey or understorey. The stomatal conductance g_{si} for a vegetation layer is calculated using Eqs. (A30)–(A35) in Appendix A.5. As the wind speed is not used, we set the aerodynamic resistance r_{ai} to be 5.0 s m^{-1} for the overstorey, 15.0 s m^{-1} for the understorey, and 30.0 s m^{-1} for moss.

When water evaporates from wet surfaces, r_{ci} is set to zero for the vegetation layers, and therefore the evaporation (E_{wi}) of the wet vegetation surface is estimated from:

$$E_{wi} = \frac{\Delta R_{ni} + \rho c_p \frac{e_s - e}{r_{ai}}}{\lambda_v (\Delta + \gamma)} \delta t \tag{A6}$$

Evaporation of the intercepted water in a layer is taken as the minimum of the potential rate and the intercepted rainfall:

$$E_{ai} = \min(E_{wi}, S_{ti}) \tag{A7}$$

Given Eqs. (A4)–(A7), the total actual evapotranspiration from a canopy (E_{ci}) is:

$$ET_{ci} = E_{ai} + E_{ti} \tag{A8}*$$

It is assumed that transpiration can occur on wet leaf surfaces, i.e. the transpiration and evaporation can occur in parallel. This is a simplification of the original model.

Evaporation from wet moss is estimated using the same procedure with relevant values for the different variables as the moss/litter layer in the original model, but the moss surface resistance (r_{ci} in s m^{-1}) to the vapor flux is related to the storage of the moss surface (M_w) using the following relationships (Williams and Flanagan, 1998)

$$r_{ci} = 0.5\left(\frac{1}{g_{c,Sphag}} + \frac{1}{g_{c,Pleur}}\right) \quad \text{(A9)}^{**}$$

$$g_{c,Sphag} = -0.195 + 0.134M_w - 0.0256M_w^2 + 0.00228M_w^3 - 0.0000984M_w^4 + 0.00000168M_w^5 \quad \text{(A10)}^{**}$$

$$g_{c,Pleur} = -0.0194 + 0.021M_w - 0.00446M_w^2 + 0.000455M_w^3 - 0.0000248M_w^4 + 0.000000592M_w^5 \quad \text{(A11)}^{**}$$

where $g_{c,Sphag}$ and $g_{c,Pleur}$ are the surface conductances (m s^{-1}) of *Sphagnum* and *Pleurozium* moss layers, respectively. Taking the suggested values of $M_w = 17$ for *Sphagnum* and $M_w = 12$ for *Pleurozium*, r_{ci} is estimated from Eqs. (A9)–(A11) assuming these two moss types have equal spatial coverages.

Evaporation from moss and soil (E_s) as a total layer is calculated with climate-controlled or soil-controlled conditions (Eagleson, 1978):

$$E_s = \min(E_{ps}, F_s) \quad \text{(A12)}^{*}$$

where E_{ps} is the potential evaporation of soil/moss surface and is estimated using Eq. (A4) with r_{ci} calculated from Eqs. (A9)–(A11). In the absence of moss, it can be replaced by a soil resistance r_s (Choudhury and Monteith, 1988). In general, it can be weighted by the percent moss cover. In this study, we assume 100% moss cover. Although moss has quasi-stomatal control on evaporation, it consumes water only through capillary rise in rain-free periods. It is therefore also controlled by the soil as expressed in Eq. (A13). F_s is called the soil-controlled exfiltration volume or depth and is calculated as

$$F_s = S_e t^{-1/2} \quad \text{(A13)}$$

where S_e is soil desorptivity (m d$^{-1/2}$), which is calculated using the method of Entekhabi and Eagleson (1989)

$$S_e = \left[\frac{8\Phi K_{sat0}\phi_b}{3(1+3m)(1+4m)}\right]^{1/2} S_0^{((m/2)+2)} \quad \text{(A14)}$$

where Φ is the effective soil porosity; K_{sat0} is the saturated hydraulic conductivity at the surface; m is a pore size distribution index. The values of Φ and m depend on soil texture, and can be obtained from Stieglitz et al. (1997) and Campbell and Norman (1998). ϕ_b is the soil bubbling pressure. The soil bubbling pressure equals to the soil matrix potential when S_0 equals to 1 (Brooks and Corey, 1966), where S_0 is the relative soil saturation at beginning of the time step. The relation between S_0 and Φ is defined as:

$$S_0 = \frac{\theta}{\theta_s} = \frac{\theta}{\Phi} \quad \text{(A15)}$$

A.3. Soil water mass balance in the unsaturated zone

It is assumed that the horizontal redistribution of soil water is restricted in the saturated zone. In the unsaturated zone, only vertical movement of soil water can take place. If the water table ($z_{i,j}$) is less than the capillary rise distance or soil saturation deficit ($S_{i,j}$) is zero, meaning that the whole soil profile is filled with water, and unsaturated storage is reset to zero in this case. Otherwise the change in water storage in the unsaturated zone is calculated as

$$\Delta W_{unsat} = (P - P_o - P_u - R_{off} + W_{cr} - W_{pe} - T_{o,unsat} - T_{u,unsat} - E_s)\delta t \quad \text{(A16)}^{*}$$

where W_{pe} is the rate of vertical water percolation to the saturated zone; $T_{o,unsat}$ is the transpiration of the overstorey from the unsaturated zone; $T_{u,unsat}$ is the transpiration of the understorey from the unsaturated zone; W_{cr} is the upward water flow by capilliary rise; and δt is the time interval of calculation. W_{pe} is computed from

$$W_{pe} = \begin{cases} \min(K_{unsat}(z)\delta t, \theta_{unsat} - \theta_{fc}), & \text{if } \theta_{unsat} > \theta_{fc} \\ 0, & \text{else} \end{cases} \quad \text{(A17)}$$

where $K_{unsat}(z)$ is the unsaturated hydraulic conductivity. θ_{fc} is the field capacity of the unsaturated zone and is estimated following Saxton et al. (1986) with an assumption that the water potential equals 10 kPa at the field capacity. $K_{unsat}(z)$ is estimated from:

$$K_{unsat}(z) = K_{sat}(z)\left(\frac{\theta}{\theta_s}\right)^{2b+3} \quad \text{(A18)}$$

where $K_{sat}(z)$ is the saturated hydraulic conductivity, θ is the volumetric water content, θ_s is the saturation water content, z is the water table depth from the surface, b is a soil parameter which represents the exponent of the moisture release equation:

$$\psi_m = \psi_e \left(\frac{\theta}{\theta_s}\right)^{-b} \tag{A19}$$

where ψ_m is the water matric potential, and ψ_e is the air entry water potential. The values of $K_{sat}(z)$, b and ψ_e depend on soil physical properties such as texture, and they are cited in the model from Campbell and Norman (1998). The relationship among the three soil parameters can also be expressed by equation

$$K_{sat}\psi_e^n = M \tag{A20}$$

where M is a constant.

W_{cr} is set at zero when the unsaturated zone is above the water holding capacity and otherwise calculated using the method based on Eagleson (1978)

$$W_{cr} = K_{sat}(z)\left(1 + \frac{1.5}{c-1}\right)\left(\frac{\psi_m}{z_s - \psi_m}\right)^c \tag{A21}$$

where $c = 2 + 3/b$ and b is the pore size index.

Potential unsaturated drainage (W_d) is calculated as follows

$$W_d = \begin{cases} K_{sat}(z)0.01, & C > 0.5 \\ K_{sat}(z)C, & C < 0.5 \end{cases} \tag{A22}$$

and

$$C = \begin{cases} \left(\frac{\theta_{unsat}}{\Delta W_{sat}}\right)^{2b+3} & \Delta W_{sat} > 0.01 \\ 1 & \Delta W_{sat} < 0.01 \end{cases} \tag{A23}$$

where θ_{unsat} is the water storage in the unsaturated zone, ΔW_{sat} is the saturation deficit.

A.4. Water balance in the saturated zone

In addition to the vertical processes described above, the horizontal redistribution of soil water takes place in the saturated zone. The change of water storage in the saturated zone is

$$\Delta S_{ij} = \left[\left(W_{pe,ij} + \frac{Q_{in,ij} - Q_{out,ij}}{A_{ij}}\right) - (T_{o,sat} - T_{u,sat} - W_{cr})\right]\delta t \tag{A24}*$$

where $W_{pe,ij}$ is percolation from unsaturated zone (the subscripts i and j denote pixel (i,j)); $Q_{in,ij}$ is the total subsurface saturated inflow from upslope neighboring pixels to pixel (i,j); $Q_{out,ij}$ is the total drainage from the pixel to downslope neighboring pixels, $T_{o,sat}$ and $T_{u,sat}$ are the transpiration of the overstorey and understorey from the saturated zone, respectively; and A_{ij} is the area of the pixel. $Q_{in,ij}$ and $Q_{out,ij}$ can either be calculated from 3×3 pixels or from watershed networks.

The change in water table is calculated from

$$z_{ij}^{t+\Delta t} = z_{ij}^t - \frac{\Delta S_{ij}}{(\theta_{sij} - \theta_{ij})} \tag{A25}*$$

where, $z_{ij}^{t+\Delta t}$ is the water table depth at the current time step, z_{ij}^t is the water table at the previous time step, θ_{sij} is the saturated soil moisture content, and θ_{ij} is the current average moisture content above the water table.

Each pixel can exchange water with its eight adjacent neighbors (see Fig. 3). Elevation or ground surface slope determines the direction of the water flow. A given pixel thus will receive water from its upslope neighbors and discharge to its downslope neighbors. There were up to eight directions of water output or input for a pixel. The flow direction is determined from the gradients in height from a pixel in question to downslope or upslope pixels. Along the direction with the steepest gradient among the eight neighboring pixels, the quantity of subsurface flow was the highest. For example, the rate of saturated subsurface flow at time t from pixel (i,j) to its downslope neighbors is equal to

$$Q_{ijk} = \begin{cases} T_{ij}\beta_{ijk}w_{ijk}, & \beta_{ijk} < 0 \\ 0, & \beta_{ijk} \geq 0 \end{cases} \tag{A26}$$

where T_{ij} is the hydraulic tansmissivity ($m^2\ d^{-1}$); β_{ijk} is the elevation gradient difference in the k direction; and w_{ijk} is the effective width of flow in the k direction. The total saturated subsurface outflow from pixel (i,j) to its downslope neighbors ($Q_{out,ij}$) and total

saturated subsurface inflow from upslope neighbors to pixel (i,j) ($Q_{\text{in},ij}$, $\text{m}^3\,\text{d}^{-1}$) are approximated through the summation for all neighboring pixels

$$Q_{\text{out},ij} = T_{ij}\sum_{k=1}^{8}|\beta_{ijk}|w_{ijk},\quad \beta_{ijk}<0 \qquad \text{(A27)*}$$

$$Q_{\text{in},ij} = T_{ij}\sum_{k=1}^{8}\beta_{ijk}w_{ijk},\quad \beta_{ijk}\geq 0 \qquad \text{(A28)}$$

where the hydraulic transmissivity T_{ij} is defined as

$$T_{ij} = K_{\text{sat}}(z_{ij})[\exp(-f_{ij}z_{ij}) - \exp(-f_{ij}D_{ij})]/f_{ij} \qquad \text{(A29)}$$

where $K_{\text{sat}}(z)$ is the saturated hydraulic conductivity at water table z_{ij}; D_{ij} is the total soil depth; and f_{ij} is a parameter related to the decay of saturated conductivity with depth (m^{-1}).

A.5. Stomatal conductance as a modified function of soil water content

Leaf stomatal behavior plays a key role in the transpiration control in the atmosphere–plant–soil system. A number of factors have been recognized to influence stomatal conductance or stomatal resistance, such as atmospheric variables (solar radiation, temperature, vapor pressure deficit, CO_2 concentration), plant parameters (leaf water potential, leaf area index) and soil properties (soil water content, soil water potential). In the original model, the stomatal conductance remains at the maximum value at soil water contents equal to or larger than the field capacity. In order to simulate the performance of vegetation in low areas under periodic water logging conditions, we modified one of the stomatal control functions as follows

$$g_s = \max(g_{\max}f(F_p)f(T)f(D_v)f(\theta_{sw}), g_{\min}) \qquad \text{(A30)*}$$

where $g_{\max}$ is cover type specific maximum stomatal conductance (g_s), F_p is the photosynthetic photo flux density (PPDF), T is temperature, D_v is vapor pressure deficit and θ_{sw} is soil water content. This modification is made according to a daily canopy photosynthesis model (Chen et al., 1999) employing a surface conductance model (Jarvis, 1976; Stewart, 1988)

$$f(F_p) = \frac{F_c F_p}{1 + F_c F_p} \qquad \text{(A31)*}$$

$$f(T) = \begin{cases} \dfrac{\ln(T)}{\ln(T_{\text{opt}})}, & T \leq T_{\text{opt}} \\ \cos\left(\dfrac{\pi}{2}\dfrac{(T - T_{\text{opt}})}{T_{\max} - T_{\text{opt}}}\right), & T > T_{\text{opt}} \\ 0, & T \leq 1 \end{cases} \qquad \text{(A32)*}$$

$$f(D_v) = \begin{cases} 1, & D_v \leq D_{\text{open}} \\ \dfrac{D_{\text{close}} - D_v}{D_{\text{close}} - D_{\text{open}}}, & D_{\text{open}} < D_v < D_{\text{close}} \\ 0, & D_v \geq D_{\text{close}} \end{cases} \qquad \text{(A33)*}$$

$$f(\theta_{sw}) = \begin{cases} 0, & \theta_{sw}(z) \leq \theta_{wp} \\ \dfrac{\theta_{sw}(z) - \theta_{wp}}{\theta_{fc}(z) - \theta_{wp}}, & \theta_{wp} < \theta_{sw}(z) \leq \theta_{fc}(z) \\ 1 - 0.5\dfrac{\theta_{sw}(z) - \theta_{fc}(z)}{\theta_s(z) - \theta_{fc}(z)}, & \theta_{fc}(z) < \theta_{sw}(z) \leq \theta_s(z) \end{cases} \qquad \text{(A34)*}$$

where F_c is a coefficient in the relationship between g_s and F_p with a fixed value of 0.01 $\mu\text{mol}\,\text{m}^{-2}\,\text{s}^{-1}$; T_{opt} is the optimal temperature, taken as 25 °C; $T_{\max}$ is the maximum temperature at which plants stop photosynthesizing, taken as 40 °C; D_{open} is the vapour pressure deficit at which stomata are fully open, taken as 0.2 kPa (Dang et al., 1997); D_{close} is the vapour pressure deficit at stomatal closure, taken as 3 kPa (Dang et al., 1997); θ_{wp} is the permanent wilting point; $\theta_{sw}(z)$ is the soil water content at depth z; $\theta_{fc}(z)$ is the field capacity at depth z; and $\theta_s(z)$ is the soil saturated water content at depth z. Eq. (A34) is a main adjustment to the original Wigmosta's model to consider the effect of the decrease in root activities under anaerobic conditions when $\theta_{sw}(z)$ exceeds $\theta_{fc}(z)$ by assuming that $f(\theta_{sw})$ decreases from unity at the field capacity to 0.5 at saturation. Various studies (Kozlowski, 1984; Zhang and Davies, 1986; Else et al., 1996) provide evidence that either stomatal conductance decreases or transpiration decreases with increasing θ_{sw} beyond θ_{fc}.

For the total PPFD (both direct and diffuse) for the overstorey and understorey required by Eq. (A31), the direct and diffuse solar irradiances calculated at each layer by Eqs. (A45)–(A55) are converted to PPDF with a conversion factor of 2.0 ($\mu\text{mol}\,\text{m}^{-2}\,\text{s}^{-1}$)/($\text{W}\,\text{m}^{-2}$) (Landsberg and Waring, 1997).

Table A1
Values of short-wave radiation albedos and stomatal conductance[a]

Symbol	Variable	Conifer forest	Deciduous forest	Mixed forest	Grass
$\alpha_{o,b}$	Direct radiation albedo of overstorey	0.14	0.15	0.15	0.21
$\alpha_{u,b}$	Direct radiation albedo of understorey	0.15	0.16	0.16	0.22
$\alpha_{g,b}$	Direct radiation albedo of ground	0.15	0.16	0.16	0.22
$\alpha_{o,d}$	Diffuse radiation albedo of overstorey	0.14	0.15	0.15	0.21
$\alpha_{u,d}$	Diffuse radiation albedo of understorey	0.15	0.16	0.16	0.22
$\alpha_{g,d}$	Diffuse radiation albedo of ground	0.15	0.16	0.16	0.22
g_{max} (mm s^{-1})	Maximum stomatal conductance	1.6	2.5	2.0	5.0

[a] The values of albedo are determined based on Sellers et al. (1997), Stieglitz et al. (1997), and Waring and Running (1998); the values of maximum canopy conductance are from Liu et al. (2002).

The values of the variables in these equations are found in Tables A1 and A2.

A.6. Root zone, unsaturated zone and saturated zone

Generally, the unsaturated zone and saturated zone are variable with time as the water table changes seasonally, but the root zone remains about the same. In other words, the rooting zone may not be limited in the unsaturated zone and the saturated zone can extend to the root zone in rainy periods. Therefore, transpiration extracts water from either the unsaturated or saturated zone, or both depending on the time in the growing season. In order to simulate the mean soil water content in the root zone, we need to make a distinction between the unsaturated zone and root zone.

To separate transpiration for saturated and unsaturated zones, the pattern of root vertical distribution within the soil profile is needed. It has been reported that nearly 95% of roots are located in the top 1.0 m of soil (Jackson et al., 1996) and the root vertical distribution down the soil profile is triangular in form, suggesting that root indexes (root number, volume, density, biomass, etc.) decrease with increasing depth from the surface. Therefore, the root vertical distribution relative to soil depth can be described as follows (Gale and Grigal, 1987)

$$f(r) = r_j = 1 - \beta^{z_j} \quad \text{(A35)**}$$

where $f(r)$ describes the root vertical distribution within the soil profile; r_j is the cumulative root fraction (a faction between 0 and 1) from the soil surface to depth z_j (cm); and β is the fitted extinction coefficient. High values of β (e.g. 0.98) indicate a larger proportion of roots at deeper soil depths, and low β values (e.g. 0.92) imply a larger proportion of roots near the soil surface. Jackson et al. (1996) showed that the average β value for boreal forests is 0.943, and that 83% root biomass is in the upper 30 cm, and that mean root biomass density is 2.9 kg m^{-2} in this forest ecosystem.

In the present model, the root distribution function $f(r)$ is used to differentiate the total transpired water into saturated and unsaturated components. According to the pipe theory, we can assume that

Table A2
Threshold values for stomatal conductance calculation

Symbol	Description	Value	Unit	Reference
F_c	Coefficient in a relationship between g_s and PPFD	0.01	μmol m^{-2} s^{-1}	Kimball et al. (1997)
T_{opt}	Optimal temperature	25	°C	Kimball et al. (1997)
T_{range}	Maximum temperature range	40	°C	Kimball et al. (1997)
D_{open}	Vapour pressure deficit at stomatal opening	0.2	kPa	Dang et al. (1997)
D_{close}	Vapour pressure deficit at stomatal closure	3.0	kPa	Dang et al. (1997)
θ_{wp}	Permanent wilting point	3.0	%	This study
θ_{sc}	Soil saturated water content	80.0	%	This study

the proportion of leaves that are influenced by roots in a soil zone equals the fraction of roots in the same zone. With this assumption, the two transpiration components can be calculated as:

(1) for the unsaturated zone:

$$g_{si-\mathrm{unsat}} = \max(g_{\mathrm{max}i} f(F_\mathrm{p}) f(T) f(D_\mathrm{v}) f(\theta_\mathrm{unsat}), g_\mathrm{min}) \quad \text{(A36)*}$$

and

$$T_{i,\mathrm{unsat}} = (1-\beta^{z_i}) T(g_{si-\mathrm{unsat}}) \quad \text{(A37)**}$$

(2) for the saturated zone:

$$g_{si-\mathrm{sat}} = \max(g_{\mathrm{max}i} f(F_\mathrm{p}) f(T) f(D_\mathrm{v}) f(\theta_\mathrm{sat}), g_\mathrm{min}) \quad \text{(A38)*}$$

and

$$T_{i,\mathrm{sat}} = \beta^{z_i} T(g_{si-\mathrm{sat}}) \quad \text{(A39)**}$$

where θ_unsat and θ_sat are the soil moisture contents for the unsaturated and saturated zones, respectively; $g_{si\text{-}\mathrm{unsat}}$ and $g_{si\text{-}\mathrm{sat}}$ are the stomatal conductances calculated based on θ_sw in the unsaturated and saturated zones, respectively; and $T(g_{si\text{-}\mathrm{unsat}})$ and $T(g_{si\text{-}\mathrm{sat}})$ are the transpiration from the two zones, respectively, calculated with Eq. (A4) with $1/r_{ci}$ substituted by the stomatal conductance. The subscript i is for overstorey or understorey transpiration.

A.7. Solar radiation on sloping surfaces

At each time step (e.g. hour), day of the year, and location (i.e. latitude and longitude), solar azimuth (β_z) and zenith (θ_s) angles can be calculated from

$$\beta_z = \mathrm{Arc\ tan}\left(\frac{(1.0-Z^2)^{1/2}}{Z}\right) \quad \text{(A40)**}$$

where $Z = \cos\theta_s$, defined according to the solar time (T_s), declination (D_s) and latitude(ϕ):

$$\cos\theta_s = \sin(\varphi\pi/180)\sin(D_s) + \cos(\varphi\pi/180)\cos(D_s)\cos((T_s-12)\varphi\pi/(180\times 12)) \quad \text{(A41)**}$$

One simple way to quantify the influence of topography on the surface radiation budget is to consider the geometry between the solar beam and the normal to the slope (Campbell and Norman, 1988):

$$L_\mathrm{r} = \cos(\beta_\mathrm{sl}-\beta_z)\sin\theta_\mathrm{sl}\sin\theta_s + \cos\theta_\mathrm{sl}\cos\theta_s \quad \text{(A42)**}$$

where L_r is the projection of a solar beam on the sloping surface (scaled 0.0–1.0), and β_sl and θ_sl are the aspect and slope of a pixel, respectively.

From measured global solar radiation (S_g) on a horizontal surface, we first separate direct and diffuse components using Eqs. (A45)–(A47) (Appendix A.8). The ratio of the direct solar irradiance between a sloping pixel and a horizontal surface is determined by:

$$R_\mathrm{slope} = \frac{L_\mathrm{r}}{\sin(\theta_\mathrm{se})}, \quad \theta_\mathrm{se} > 0 \quad \text{(A43)**}$$

This ratio is applied to the direct radiation component. The diffuse radiation would vary with slope to a much smaller extent because as the slope increases, the diffuse radiation from the sky decreases but this decrease is more or less compensated by the reflected radiation from surrounding terrain (Chen et al., 1993). For simplicity, we therefore do not adjust the diffuse component according to slope. The photosynthetic photon flux density (F_p) of on the top of overstorey on slope is then obtained through the following conversion

$$F_\mathrm{p} = C_\mathrm{r}(R_\mathrm{slope} S_\mathrm{dir} + S_\mathrm{dif}) \quad \text{(A44)**}$$

where C_r is a conversion factor from total solar radiation to photosynthetically active radiation, taken as 2.0 ($\mu\mathrm{mol\ m^{-2}\ s^{-1}}$)/($\mathrm{Wm^{-2}}$) (Landsberg and Waring, 1997). S_dir and S_dif are direct and diffuse irradiance, respectively.

A.8. Net radiation of vegetation layers and soil surface

In forests, there is often an understorey layer consisting of grass and shrubs in between the overstorey (forest canopy) and the moss layer. According to our previous work (Chen, 1996; Chen et al., 1999), we developed the following canopy radiation module to consider the effects of different canopy architectures in different vegetation functional types on radiation balance of both overstorey and understorey as well as the underlying moss/litter/soil surface. The module consists of three components: direct incoming

solar radiation ($R_{\mathrm{dir},i}$), diffuse solar radiation ($R_{\mathrm{dif},i}$) and long wave radiation ($R_{\mathrm{l},i}$), i.e.

$$R_{\mathrm{n},i} = R_{\mathrm{dir},i} + R_{\mathrm{dif},i} + R_{\mathrm{l},i} \quad \text{(A45)}^{**}$$

The partition of incoming solar radiation into direct and diffuse components is done using the following empirical equations for high latitude unpolluted air (Chen et al., 1999)

$$\frac{S_{\mathrm{dif}}}{S_{\mathrm{g}}} = \begin{cases} 0.943 + 0.734R - 4.9R^2 \\ \qquad +1.796R^3 + 2.058R^4, & R < 0.8 \\ 0.13, & R \geq 0.8 \end{cases} \quad \text{(A46)}^{**}$$

where S_{g} is the incoming global radiation in W m^{-2}. The parameter R is defined as:

$$R = \frac{S_{\mathrm{g}}}{S_0 \cos\theta} \quad \text{(A47)}^{**}$$

where S_0 and θ are the solar constant (1380 W m^{-2}) and solar zenith angle, respectively.

Direct radiation above the canopy (S_{dir}) is the remainder of incoming global radiation minus the diffuse radiation estimated from Eq. (A46). Methods to estimate the attenuation of diffuse and direct radiation in the canopy are further developments from Chen et al. (1999). The direct irradiance absorbed by the vegetation layers and the ground, at a given time of the day or solar zenith angle θ, is calculated as follows

$$R_{\mathrm{dir,o}} = S_{\mathrm{dir}}\left[(1-\alpha_{\mathrm{o},b}) - (1-\alpha_{\mathrm{u},b})\mathrm{e}^{-(0.5L_{\mathrm{o}}\Omega_{\mathrm{o}})/\cos\theta}\right] \quad \text{(A48)}^{**}$$

$$R_{\mathrm{dir,u}} = S_{\mathrm{dir}}\,\mathrm{e}^{-(0.5L_{\mathrm{o}}\Omega_{\mathrm{o}})/\cos\theta}\left[(1-\alpha_{\mathrm{u},b}) - (1-\alpha_{\mathrm{g},b})\mathrm{e}^{-(0.5L_{\mathrm{u}}\Omega_{\mathrm{u}})/\cos\theta}\right] \quad \text{(A49)}^{**}$$

$$R_{\mathrm{dir,g}} = S_{\mathrm{dir}}\,\mathrm{e}^{-0.5(L_{\mathrm{o}}\Omega_{\mathrm{o}}+L_{\mathrm{u}}\Omega_{\mathrm{u}})/\cos\theta}(1-\alpha_{\mathrm{g},b}) \quad \text{(A50)}^{**}$$

where $R_{\mathrm{dir,o}}$, $R_{\mathrm{dir,u}}$ and $R_{\mathrm{dir,g}}$ are the direct irradiance absorbed by overstorey, understorey and ground surface, respectively. L_{o} and L_{u} are the leaf area indices of the overstorey and understorey canopy, respectively. Variables $\alpha_{\mathrm{o},b}$, $\alpha_{\mathrm{u},b}$ and $\alpha_{\mathrm{g},b}$ are the albedos of the overstorey, understorey and ground surface for direct radiation, respectively. Ω_{o} and Ω_{u} are the clumping indices for the overstorey and understorey, respectively.

For daily step calculations, Eqs. (A48)–(A50) need to be integrated for the whole range of the solar zenith angle from noon to sunset (Liu et al., 1997). For Eq. (A50), the daily integrated results are

$$\begin{aligned} R_{\mathrm{dir,o,daily}} &= S_{\mathrm{dir}}\left[(1-\alpha_{\mathrm{o},b}) - (1-\alpha_{\mathrm{o,u}})\right. \\ &\quad \left.\times\left(\int_{\theta_{\mathrm{noon}}}^{2/\pi} p(\theta)\cos\theta\,\mathrm{d}\theta\right)\Big/\left(\int_{\vartheta_{\mathrm{noon}}}^{2/\pi}\cos\theta\,\mathrm{d}\theta\right)\right] \\ &= S_{\mathrm{dir}}\left[(1-\alpha_{\mathrm{o},b}) - (1-\alpha_{\mathrm{o,u}})\right. \\ &\quad \left.\times P(\theta_{\mathrm{noon}})\frac{\cos\theta_{\mathrm{noon}} - \left(\frac{\pi}{2}-\theta_{\mathrm{noon}}\right)\sin\theta_{\mathrm{noon}}}{\left(\frac{\pi}{2}-\theta_{\mathrm{noon}}\right)(1-\sin\theta_{\mathrm{noon}})}\right] \end{aligned} \quad \text{(A51)}^{**}$$

$$P(\theta_{\mathrm{noon}}) = \mathrm{e}^{-(0.5\Omega L_{\mathrm{o}})/\cos\theta_{\mathrm{noon}}} \quad \text{(A52)}^{**}$$

where S_{dir} is the daily total direct solar radiation from the atmosphere in J m^{-2} day^{-1}; θ_{noon} is the solar zenith angle at noon and is a function of latitude and day of year; and $P(\theta_{\mathrm{noon}})$ is the gap fraction at noon. For the understorey component described in Eq. (A49), a similar integration is done. Eq. (A50) is also adjusted to use the daily integration results for the overstorey and understorey.

The diffuse radiation originates from two sources: sky irradiance and multiple scattering of the incident radiation within the canopy. The diffuse irradiances for the layers are computed as follows

$$R_{\mathrm{dif,o}} = S_{\mathrm{dif}}\left[(1-\alpha_{\mathrm{o,d}}) - (1-\alpha_{\mathrm{u,d}})\mathrm{e}^{-(0.5L_{\mathrm{o}}\Omega_{\mathrm{o}})/\cos\bar{\theta}_{\mathrm{o}}}\right] + 0.07\Omega_{\mathrm{o}}S_{\mathrm{dir}}(1.1-0.1L_{\mathrm{o}})\mathrm{e}^{-\cos\theta} \quad \text{(A53)}^{**}$$

$$R_{\mathrm{dif,u}} = S_{\mathrm{dif}}\,\mathrm{e}^{-(0.5L_{\mathrm{o}}\Omega_{\mathrm{o}})/\cos\bar{\theta}_{\mathrm{o}}}\left[(1-\alpha_{\mathrm{u,d}}) - (1-\alpha_{\mathrm{g,d}})\mathrm{e}^{-(0.5L_{\mathrm{u}}\Omega_{\mathrm{u}})/\cos\bar{\theta}_{\mathrm{u}}}\right] + 0.07\Omega_{\mathrm{u}}S_{\mathrm{dir}}\,\mathrm{e}^{-(0.5L_{\mathrm{o}}\Omega_{\mathrm{o}})/\cos\theta}(1.1-0.1L_{\mathrm{u}})\mathrm{e}^{-\cos\theta} \quad \text{(A54)}^{**}$$

$$R_{\mathrm{dif,g}} = S_{\mathrm{dif}}\, \mathrm{e}^{-0.5(L_{\mathrm{o}}\Omega_{\mathrm{o}}+L_{\mathrm{u}}\Omega_{\mathrm{u}})/\cos\bar{\theta}_{\mathrm{u}}}(1-\alpha_{\mathrm{g,d}}) \quad \text{(A55)}^{**}$$

where $R_{\mathrm{dif,o}}$, $R_{\mathrm{dif,u}}$ and $R_{\mathrm{dif,g}}$ are diffuse irradiances in overstorey and understorey and on the ground surface, respectively; $\alpha_{\mathrm{o,d}}$, $\alpha_{\mathrm{u,d}}$ and $\alpha_{\mathrm{g,d}}$ are albedos for diffuse radiation in the three layers, respectively (values see Table A1); and $\bar{\theta}_{\mathrm{o}}$ and $\bar{\theta}_{u}$ are representative zenith angles for diffuse radiation transmission through the vegetation layers, and depend slightly on leaf area index, i.e.

$$\cos\bar{\theta}_{\mathrm{o}} = 0.537 + 0.025L_{\mathrm{o}} \quad \text{(A56)}^{**}$$

$$\cos\bar{\theta}_{\mathrm{u}} = 0.537 + 0.025L_{\mathrm{u}} \quad \text{(A57)}^{**}$$

The representative angle for diffuse radiation transmission is derived through numerical simulations with the assumption of isotropic sky radiance (Chen et al., 1999).

With the assumption that the daily-mean temperatures of the overstorey and understorey are the same as the air temperature, the balance of longwave radiation is described as follows

$$\begin{aligned} R_{\mathrm{l,o}} = {} & \varepsilon_{\mathrm{o}}\Big[\varepsilon_{\mathrm{a}}\sigma T_{\mathrm{a}}^4 + \varepsilon_{\mathrm{u}}\sigma T^4(1-\mathrm{e}^{-(0.5L_{\mathrm{u}}\Omega_{\mathrm{u}})/\cos\bar{\theta}_{\mathrm{u}}}) \\ & + \varepsilon_{\mathrm{g}}\sigma T_{\mathrm{g}}^4\, \mathrm{e}^{-(0.5L_{\mathrm{u}}\Omega_{\mathrm{u}})/\cos\bar{\theta}_{\mathrm{u}}} - 2\varepsilon_{\mathrm{o}}\sigma T_{\mathrm{a}}^4\Big] \\ & \times(1-\mathrm{e}^{-(0.5L_{\mathrm{o}}\Omega_{\mathrm{o}})/\cos\bar{\theta}_{\mathrm{o}}}) \end{aligned} \quad \text{(A58)}^{**}$$

$$\begin{aligned} R_{\mathrm{l,u}} = {} & \varepsilon_{\mathrm{u}}\Big[\varepsilon_{\mathrm{a}}\sigma T_{\mathrm{a}}^4\mathrm{e}^{-(0.5L_{\mathrm{o}}\Omega_{\mathrm{o}})/\cos\bar{\theta}_{\mathrm{o}}} \\ & + \varepsilon_{\mathrm{o}}\sigma T_{\mathrm{a}}^4(1-\mathrm{e}^{-(0.5L_{\mathrm{o}}\Omega_{\mathrm{o}})/\cos\bar{\theta}_{\mathrm{o}}}) \\ & + \varepsilon_{\mathrm{g}}\sigma T_{\mathrm{g}}^4 - 2\varepsilon_{\mathrm{u}}\sigma T_{\mathrm{a}}^4\Big](1-\mathrm{e}^{-(0.5L_{\mathrm{u}}\Omega_{\mathrm{u}})/\cos\bar{\theta}_{\mathrm{u}}}) \end{aligned} \quad \text{(A59)}^{**}$$

$$\begin{aligned} R_{\mathrm{l,g}} = {} & \varepsilon_{\mathrm{g}}\Big[\varepsilon_{\mathrm{a}}\sigma T_{\mathrm{a}}^4\, \mathrm{e}^{-(0.5L_{\mathrm{o}}\Omega_{\mathrm{o}})/\cos\bar{\theta}_{\mathrm{o}}} \\ & + \varepsilon_{\mathrm{o}}\sigma T_{\mathrm{a}}^4(1-\mathrm{e}^{-(0.5L_{\mathrm{o}}\Omega_{\mathrm{o}})/\cos\bar{\theta}_{\mathrm{o}}})\Big]\mathrm{e}^{-(0.5L_{\mathrm{u}}\Omega_{\mathrm{u}})/\cos\theta_{\mathrm{u}}} \\ & + \varepsilon_{\mathrm{u}}\sigma T_{\mathrm{a}}^4(1-\mathrm{e}^{-(0.5L_{\mathrm{u}}\Omega_{\mathrm{u}})/\cos\bar{\theta}_{\mathrm{u}}}) - \varepsilon_{\mathrm{g}}\sigma T_{\mathrm{g}}^4 \end{aligned} \quad \text{(A60)}^{**}$$

where ε_{a}, ε_{o}, ε_{u} and ε_{g} are emissivities of the atmosphere, overstorey, understorey and ground surface, respectively. Pre-described values of 0.98, 0.98 and 0.95 are assigned to ε_{o}, ε_{u} and ε_{g} (Chen and Zhang, 1989; Chen et al., 1989), respectively, but ε_{a} is computed as $\varepsilon_{\mathrm{a}} = 1.24(e_{\mathrm{a}}/T_{\mathrm{a}})^{1/7}$ (Brutseart, 1982), where e_{a} and T_{a} are water vapor pressure and temperature of the atmosphere.

On sloping surfaces, the solar zenith angle in the above equations should be replaced by the angle of the solar beam to the normal to the surface, i.e. replacing θ_{s} with

$$\theta_{\mathrm{ss}} = \cos^{-1}(L_{\mathrm{r}}) \quad \text{(A61)}^{**}$$

where L_{r} is defined in Eq. (A42).

The direct and diffuse solar irradiances calculated by Eqs. (A48)–(A55) are used to obtain PPFD for the overstorey and understorey based on Eq. (A45). PPFD for each vegetation layer is needed for canopy conductance estimation using Eq. (A31).

References

Abbott, M.B., Refsgaard, J.C., 1996. Distributed Hydrological Modelling. Kluwer Academic Publishers, The Netherlands.

Acton, D.F., Padbury, G.A., Shields, J.A., 1991. Soil Landscapes of Canada-Saskatchewan Digital Map Data; Scale 1:1,000,000; CanSIS No. SK018200, version 90.11.30; CLBRR Archive, Agriculture Canada, Research Branch, Ottawa, Canada. (CLBRR Contribution No. 91-107D).

Baldocchi, D., 1997. Measuring and modeling carbon dioxide and water vapour exchange over a temperate broad leaved forest during the summer drought. Plant Cell Environment 20, 1108–1122.

Band, L.E., Patterson, P., Nemani, R., Running, S.W., 1993. Forest ecosystem processes at the watershed scale: incorporating hillslope hydrology. Agricultural and Forest Meteorology 63, 93–126.

Barber, D.G., Hochheim, P., Dixon, R., Mosscrop, D.R., McMullan, M.J., 1997. The role of earth observation technologies in flood mapping: a Manitoba case study. Canadian Journal of Remote Sensing 22, 137–143.

Baumgartner, M.F., Apfl, G., 1994. Towards an integrated geographic analysis system with remote sensing, GIS and consecutive modeling for snow cover monitoring. International Journal of Remote Sensing 15 (7), 1507–1518.

Beaujouan, V., Durand, P., Ruiz, L., Aurousseau, P., Cotteret, G., 2002. A hydrological model decicated to topography-based simulation of nitrogen transfer and transformation: rationale and application to the geomorphology-denitrification relationship. Hydrological Processes 16, 493–507.

Beven, K.J., Kirkby, M.J., 1979. A physically-based variable contributing area model of basin hydrology. Hydrological Science Bulletin 24, 43–69.

Branfireun, B.A., Roulet, N.T., 1998. The baseflow and storm flow hydrology of a Precambrian shield headwater peatland. Hydrological Processes 12, 57–72.

Brivio, P.A., Colombo, R., Maggi, M., Tomasoni, R., 2002. Integration of remote sensing data and GIS for accurate mapping of flooded areas. International Journal of Remote Sensing 23 (3), 429–441.

Brooks, R.H., Corey, A.T., 1966. Properties of porous media affecting fluid flow. Journal of Irrigation and Drainage American Society of Civil Engineering IR 2, 61–88.

Brutsaert, W.H., 1982. Evaporation into the Atmosphere. Reidel, Dordrecht, The Netherlands.

Campbell, G.S., Norman, J.M., 1998. Introduction to Environmental Biophysics. Springer, New York p. 286.

Chen, J.M., 1996. Evaluation of vegetation indices and a modified simple ratio for boreal applications. Canadian Journal of Remote Sensing 22, 229–242.

Chen, J.M., Cihlar, J., 1996. Retrieving leaf area index of boreal conifer forests using Landsat TM images. Remote Sensing Environment 55, 153–162.

Chen, J.M., Zhang, R.H., 1989. Studies on the measurements of crop thermal emissivity and sky temperature. Agricultural and Forest Meteorology 49, 23–34.

Chen, J.M., Yang, B.J., Zhang, R.H., 1989. Soil thermal emissivity as affected by its water content and surface treatment. Soil Science 148, 433–435.

Chen, J.M., Black, T.A., Price, D.T., Carter, R., 1993. Model for calculating photosynthetic photon flux densities in forest openings on slope. Journal of Applied Meteorology 32, 1656–1665.

Chen, J.M., Rich, P.M., Gower, S.T., Norman, J.M., Plummer, S., 1997. Leaf area index of boreal forests: theory, techniques, and measurements. Journal of Geophysical Research 102 (D24), 29429–29443.

Chen, J.M., Liu, J., Cihlar, J., Guolden, M.L., 1999. Daily canopy photosynthesis model through temporal and spatial scaling for remote sensing applications. Ecological Modelling 124, 99–119.

Chen, J.M., Chen, W., Liu, J., Cihlar, J., 2000. Annual carbon balance of Canada's forest during 1895–1996. Global Biogeochemical Cycle 14, 839–850.

Choudhury, B.J., Monteith, J.L., 1988. A four-layer model for the heat budget of homogeneous land surfaces. Quarterly Journal of the Royal Meteorological Socoety 114, 373–398.

Cihlar, J., Beaubien, J., Latifovic, R., Simard, G., 1999. Land cover of Canada 1995 Version 1.1. Digital Data Set Documentation. Natural Resource Canada, Ottawa, Ont.

Dang, Q.L., Margolis, H.A., Coyea, M.R., Sy, M., Collatz, G.J., 1997. Regulation of branch-level gas exchange of boreal trees: roles of shoot water potential and vapour pressure difference. Tree Physiology 17, 521–535.

De Jong, R., Shields, J.A., Sly, W.K., 1984. Estimated soil water reserves applicable to a wheat-fallow rotation for generalized soil areas mapped in southern Saskatchewan. Canadian Journal of Soil Science 64, 667–680.

Devito, K.J., Hill, A.R., Roulet, N.T., 1996. Groundwater-surface water interactions in heaswater forested wetlands of the Canadian Shield. Journal of Hydrology 181, 127–147.

Dickinson, R.E., Henderson-Sellers, A., Rosenzweig, C., Sellers, P.J., 1991. Evapotranspiration models with canopy resistance for use in climate models, a review. Agriculture and Forest Meteorology 54, 373–388.

Donald, J.R., 1992. Snowcover depletion curves and satellite snowcover estimates for snowmelt runoff modeling. PhD Thesis, University of Waterloo, Waterloo, Ont., Canada.

Eagleson, P.S., 1978. Climate, soil, and vegetation, 3, a simplified model of soil moisture movement in the liquid phase. Water Resources Research 14 (5), 722–730.

Else, M.A., Tiekstra, A.E., Croker, S.J., Davies, W.J., Jackson, M.B., 1996. Stomatal closure in flooded tomato plants involveds abscisic acid and a chemically unidentified anti-transpirant in xylem sap. Plant Physiology 112, 239–247.

Engman, E.T., 1996. Remote sensing applications to hydrology: future impact. Hydrological Sciences 41, 637–647.

Entekhabi, D., Eagleson, P.S., 1989. Land surface hydrology parameterization for atmospheric general circulation models including subgrid scale spatial variability. Journal of Climate 2, 816–831.

Field, C., Bass, B., Silva Dias, M.A.F.da., Avissar, R., Becker, A., Claussen, M., 1998. Biospheric aspects of the hydrological cycle. Journal of Hydrology 212/213 (1/4), 1–21.

Gale, M.R., Grigal, D.F., 1987. Vertical root distributions of northern tree species in relation to successional status. Canadian Journal of Forest Research 17, 829–834.

Gower, S.T., Vogel, J.G., Norman, J.M., Kucharik, C.J., Steele, S.J., Stow, T.K., 1997. Carbon distribution and aboveground net primary production in aspen, jack pine, and black spruce stands in Saskatchewan and Manitoba, Canada. Journal of Geophysical Research 102 (D24), 29029–29041.

Hollenbeck, K.J., Schmugge, T.J., Homberger, G.M., Wang, J.R., 1996. Identifying soil hydraulic heterogeneity by detection of relative change in passive microwave remote sensing observations. Water Resource Research 32 (1), 139–148.

Islam, M., Sado, K., 2002. Development priority map for flood countermeasures by remote sensing data with geographic information system. Journal of Hydrologic Engineering 7 (5), 346–355.

Jackson, T.J., 1993. Measuring surface soil moisture using passive microwave remote sensing. Hydrological Processes 7 (2), 139–152.

Jackson, R.B., Canadell, J., Ehleringer, J.R., 1996. A global analysis of root distributions for terrestrial biomes. Oecologia 108, 389–411.

Jarvis, P.G., 1976. The interpretation of the variations in leaf water potential and stomatal conductance found in canopies in the field. Philosophical Transactions of the Royal Society of London, Series B 273, 593–610.

Jarvis, P.G., Massheder, J.M., Hale, S.E., Moncrieff, J.B., Rayment, M., Scott, S.L., 1997. Seasonal variation of carbon dioxide, water vapor, and energy exchanges of a boreal black spruce forest. Journal of Geophysical Research 102 (D24), 28953–28966.

Kim, G., Barros, A.P., 2002. Space-time characterization of soil moisture from passive microwave remotely sensed imagery and ancillary data. Remote Sensing of Environment 81 (2-3), 393–403.

Kimball, J.S., Thornton, P.E., White, M.A., Running, S.W., 1997. Simulating forest productivity and surface-atmosphere carbon exchange in the BOREAS study region. Tree Physiology 17, 589–599.

Kirkby, M.J., 1975. Hydrograph Modeling Strategies, in: Peel, R., Chisholm, M., Haggett, P. (Eds.), In Processes in Physical and Human Geography. Heinemann, London, pp. 69–90.

Kite, G.W., 1995. Manual for the SLURP Hydrological Model. NHRI, Saskatoon, Canada.

Kite, G.W., Kouwen, N., 1992. Watershed modeling using land classifications. Water Resources Research 28 (12), 3193–3200.

Kite, G.W., Pietroniro, A., 1996. Remote sensing applications in hydrological modeling. Hydrological Sciences 41, 563–591.

Kouwen, N., Soulis, E.D., Pietroniro, A., Donald, J.R., Harrington, R.A., 1993. Grouped response units for distributed hydrologic modeling. Journal of Water Resource Planning Management ASCE 119 (3), 289–305.

Kozlowski, T.T. (Ed.), 1984. Flooding and Plant Growth. Academic Press, New York, p. 356.

Landsberg, J.J., Waring, R.H., 1997. A generalized model of forest productivity using simplified concepts of radiation-use efficiency, carbon balance and partitioning. Forest Ecology and Management 95, 209–228.

Liu, J., Chen, J.M., Cihlar, J., Chen, W., 2002. Remote sensing based estimation of net primary productivity over Canadian landmass. Global Ecology and Biogeography 11, 115–129.

Mielke, M.S., Oliva, M.A., Barros, N.F., Penchel, R.M., Martinez, C.A., Fonseca, S., Almeida, A.C., 1999. Stomatal control of transpiration in the canopy of a clonal *Eucalyptus grandis* plantations. Trees 13, 152–160.

Mimikou, M., Kouvopolulos, Y., Cavadias, G., Vayianos, N., 1991. Regional hydrological effects of climate change. Journal of Hydrology 123, 119–146.

Mohseni, O., Stefan, H.G., 1998. A monthly streaflow model. Water Resources Research 34, 1287–1298.

Monteith, J.L., 1965. Evaporation and the environment. Proceedings of the Symposium on Experimental Biology 19, 205–234.

Mora, F., Iverson, L.R., 1998. On the sources of vegetation activity Agricultural and Forest Meteorology. International Journal of Remote Sensing 19, 1843–1871.

Nakane, K., Kohno, T., Horikoshi, T., Nakatsubo, T., 1997. Soil carbon cycling at a black spruce (*Picea mariana*) forest stand in Saskatchewan. Canadian Journal of Geophysical Research 102 (D24), 28785–28793.

Nash, L.L., Gleick, P.H., 1991. Sensitivity of streamflow in the Colorado Basin to climatic changes. Journal of Hydrology 125, 221–241.

Ouillon, S., Forget, P., Froidefond, J.M., Naudin, J.J., 1997. Estimating suspended matter concentrations from SPOT data and from field measurements in the Rhone River plume. MTS Journal 31 (2), 15–20.

Paniconi, C., Wood, E.F., 1993. A detailed model for simulation of catchment scale subsurface hydrological processes. Water Resource Research 29 (6), 1601–1620.

Parton, W.J., Scurlock, J.M.O., Ojima, D.S., Gilmanov, T.G., Scholes, R.J., Schimel, D.S., Kirchner, T., Menaut, J.C., Seastedt, T., Garcia Moya, E., 1993. Observations and modeling of biomass and soil organic matter dynamics for the grassland biome worldwide. Global Biogeochemical Cycles 7 (4), 785–809.

Pattey, E., Desjardins, R.L., St_Amour, G., 1997. Mass and energy exchanges over a black spruce forest during key periods of BOREAS 1994. Journal of Geophysical Research 102 (D24), 28967–28975.

Peck, E.L., Carroll, T.R., Maxson, R., Goodison, B., Metcalfe, J., 1997. Variability of soil moisture near flux towers in the BOREAS southern study area. Journal of Geophysical Research 102 (D24), 28,379–29,388.

Ritchie, J.C., Rango, A., 1996. Remote sensing applications to hydrology: introduction. Hydrological Sciences 41, 429–431.

Roberts, J.M., Cabral, O.M.R., Fish, G., Molion, L.C.B., Moore, C.J., Shuttleworth, W.J., 1993. Transpiration from and Amazonian rainforest calculated from stomatal conductances measurements. Agricultural and Forest Meteorology 65, 175–196.

Running, S.W., Coughlan, J.C., 1988. A general model of forest ecosystems processes for regional applications—I: hydrological balance, canopy gas exchanges and primary production processes. Ecological Modeling 42, 125–154.

Running, S.W., Hunt, E.R., 1993. Generalization of a forest ecosystem process model for other biomes, in: Ehleringer, J.R., Field, C. (Eds.), BIOMEBGC and an Application for Global Scale Models Scaling Physiological Process: Leaf to Globe. Academic Press, San Diego, CA, pp. 141–158.

Saxton, K.E., Rawls, W.J., Romberger, J.S., Papendick, R.I., 1986. Estimating generalized soil-water characteristics from texture. Soil Science Society of America Journal 50, 1031–1036.

Schmid, H.P., 2002. Footprint modeling for vegetation atmosphere exchange studies: a review and perspective. 113, 159–183.

Schultz, G.A., 1996. Remote sensing applications to hydrology: runoff. Hydrological Sciences 41, 453–475.

Sellers, P.J., Heiser, M.D., Hall, F.G., Verma, S.B., Desjardins, R.L., Schuepp, P.M., MacPherson, J.I., 1997. The impact of using area-averaged land surface properties-topography, vegetation condition, soil wetness - in calculations of intermediate scale (approximately 10 km^2) surface-atmosphere heat and moisture fluxes. Journal of Hydrology 190, 269–301.

Soares, J.V., Almeida, A.C., 2001. Modeling the water balance and soil water fluxes in a fast growing Eucalyptus plantation in Brazil. Journal of Hydrology 253, 130–147.

Stewart, J.B., 1988. Modelling surface conductance of pine forest. Agricultural and Forest Meteorology 43, 19–35.

Stieglitz, M., Rind, D., Famiglietti, J., Rosenzweig, C., 1997. An efficient approach to modeling the topographic control of surface hydrology for regional and global climate modeling. Journal of Climate 10, 118–137.

Storck, P., Bowling, L., Wetherbee, P., Lettenmaier, D., 1998. Application of a GIS-based distributed hydrology model for prediction of forest harvest effects on peak stream flow in the Pacific Northwest. Hydrological Processes 12, 889–904.

Tait, A.B., Hall, D.K., Foster, J.L., Armstring, R.L., 2000. Utilizing multiple datasets for snow-cover mapping. Remote Sensing of Environment 72 (1), 111–126.

Van Wijk, M.T., Dekker, S.C., Bouten, W., Kohsiek, W., Mohren, G.M.J., 2001. Simulation of carbon and water budgets of a Douglas-fir forest. Forest Ecology and Management 145, 229–241.

Wang, J., Price, K.P., Rich, P.M., 2001. Spatial patterns of NDVI in response to precipitation and temperature in the central Great Plains. International Journal of Remote Sensing 22 (18), 3827–3844.

Ward, R.C., Robinson, M., 2000. Principles of Hydrology. McGraw-Hill, London.

Waring, R.H., Running, S.W., 1998. Forest Ecosystems: Analysis at Multiple Scales. Academic Press Inc., San Diego, California, p. 370.

Wigmosta, M.S., Vail, L.W., Lettenmaier, D.P., 1994. A distributed hydrology-vegetation model for complex terrain. Water Resources Research 30 (6), 1665–1679.

Williams, T.G., Flanagan, L.B., 1998. Measuring and modeling environmental influences on photosynthetic gas exchange in *Sphagnum* and *Pleurozium*. Plant, Cell and Environment 21, 555–564.

Williams, M., Rastetter, E.B., Fernandes, D.N., Goulden, M.L., Shaver, G.R., Johnson, L.C., 1997. Predicating gross primary productivity in terrestrial ecosystems. Ecological Applications 7 (3), 882–894.

Williams, M., Law, B.E., Anthoni, P.M., Unsworth, M.H., 2001. Use of a simulation model and ecosystems flux data to examine carbon–water interactions in ponderosa pine. Tree Physiology 21 (5), 287–298.

Wood, E.F., Sivapalan, M., Beven, K.J., Band, L.E., 1988. Effects of spatial variability and scale with implications to hydrologic modeling. Journal of Hydrology 102, 29–47.

Zhang, J., Davies, W.J., 1987. ABA in roots and leaves of flooded pea plants. Journal of Experimental Botany 38, 649–659.

Zhang, W., Ogawa, K., Besheng, Y., Yamaguchi, Y., 2000. A monthly stream flow model for estimating the potential changes of river runoff on the projected global warming. Hydrological Processes 14, 1851–1868.